IMPROVEMENT OF THE CLINICAL UTILITY OF OPTICAL COHERENCE TOMOGRAPHY (OCT) RETINAL NERVE FIBER LAYER (RNFL) MEASUREMENT BY ESTABLISHING DATA COMPARABILITY ACROSS THE OCT TECHNOLOGY GENERATIONS AND MODELS

by

Jongsick Kim

B.S., University of Illinois at Urbana-Champaign, 2004

Submitted to the Graduate Faculty of

Swanson School of Engineering in partial fulfillment

of the requirements for the degree of

Doctor of Philosophy

University of Pittsburgh

2009

UNIVERSITY OF PITTSBURGH

SWANSON SCHOOL OF ENGINEERING

This dissertation was presented

by

Jongsick Kim

It was defended on

November 23rd, 2009

and approved by

Joel S. Schuman, MD, Professor, Department of Ophthalmology and Bioengineering

George Stetten, M.D., Ph.D., Professor, Department of Bioengineering

Gadi Wollstein, MD., Assistant Professor, Department of Ophthalmology

Dissertation Director: Hiroshi Ishikawa, MD., Assistant Professor, Department of Ophthalmology and Bioengineering

IMPROVEMENT OF THE CLINICAL UTILITY OF OPTICAL COHERENCE TOMOGRAPHY (OCT) RETINAL NERVE FIBER LAYER (RNFL) MEASUREMENT BY ESTABLISHING DATA COMPARABILITY ACROSS THE OCT TECHNOLOGY GENERATIONS AND MODELS

Jongsick Kim, PhD

University of Pittsburgh, 2009

Glaucoma is the second leading cause of blindness worldwide, which induces irreversible structural damage (retinal ganglion cell loss and retinal nerve fiber layer (RNFL) thinning) on the retina. Optical coherence tomography (OCT) provides non-contact in vivo cross-sectional imaging of the human retina, enabling microscopic RNFL thickness measurements, which have become an essential clinical measure for objective glaucoma assessment. However, with the conventional time-domain OCT (TD-OCT), its operator dependent scan registration contributes to major measurement variability.

Recently, spectral domain OCT (SD-OCT) technology has been introduced. SD-OCT provides faster scanning (up to 100x) and finer axial resolution (up to 2x) compared to TD-OCT, allowing three-dimensional (3D) volume sampling. This allows us to create a virtual OCT image along any sampling path (curved or straight), which permits virtually perfect scan registration. However, this also introduced backward measurement comparability problem in clinical ophthalmology since the RNFL thickness measured by TD-OCT and SD-OCT are not directly comparable.

Without ensuring the OCT measurement “backward-comparability”, physicians must retake baseline measurements using newer technologies. This wastes all accumulated OCT

measurements and shortens the longitudinal observation time. This is a critical limitation especially for glaucoma as it is a slow progressing disease.

The objective of this study is to improve the clinical utility of OCT RNFL measurement by establishing data comparability across the multiple OCT generations and models. First, we developed an algorithm to match the TD-OCT scan location within the corresponding 3D SD-OCT volume. Scan location matching (SLM) enabled computation of the calibration equation between TD- and SD-OCT for direct comparison of measurements. Second, the performance of the SLM method was measured using various SD-OCT devices with different spatial sampling methods. Finally, we developed a mathematical model of the retinal nerve fiber bundle distribution pattern to normalize the off-centered TD-OCT RNFL thickness to a virtually centered one. This allowed us to bring TD-OCT RNFL thickness measurements from different locations, over multiple visits to a virtually uniform location for longitudinal glaucoma progression analysis. The outcome of this study would facilitate more accurate and reliable glaucoma disease/progression detection in cross-sectional as well as longitudinal clinical settings.

TABLE OF CONTENTS

LIST OF TABLES

LIST OF FIGURES

PREFACE

The research described herein was conducted under the supervision of Dr. Hiroshi Ishikawa in the Department of Ophthalmology and Bioengineering, University of Pittsburgh, between September 2005 and November 2009.

I would like to express my genuine appreciation to Dr. Ishikawa, for his guidance, mentorship, and patience. He provided me with many opportunities to be an independent scientist and to develop my career. His creative thinking was an inspiration to me..

I express my sincere appreciation to Dr. Joel S. Schuman, Chair of the Department of Ophthalmology. He gave me a chance to join the Glaucoma Imaging Group (GIG) and supported me in the completion of my doctorate.

Dr. Gadi Wollstein, Dr. Richard A. Bilonick, and Dr. George Stetten deserve my genuine appreciation. They generously offered their expertise in the completion of my doctorate.

I express my sincere appreciation to my family in South Korea. Without their constant support I would not have been able to complete this work.

Finally, I express my genuine thanks to each of the following for their friendship and support: Hye Young Kim, Young Ho Bae, Sung Hwan Kim, Tea Soon Park, Sung Hong Park, Eul Soon Park, Jong Jin Kim, Larry Kagemann, Kyungrim Sung, Juan Xu, Lindsey S. Folio, Michelle L. Gabriele, Allison Ungar, Gregory A. Owens, Rose Carla Aubourg, Kristy Truman, and Yun Ling.

1.0 INTRODUCTION

1.1 PRINCIPLES OF OPTICAL COHERENCE TOMOGRAPHY (OCT)

Optical coherence tomography (OCT) provides microscopic cross-sectional images of living tissue in a non-contact and non-invasive fashion and has been applied to various medical fields primarily in ophthalmology. Figure 1-1A shows schematic of time domain OCT system (TD-OCT). [1-3] TD-OCT has a moving reference arm and a sample arm (e.g. eye) with a broadband light source (super-luminescent diode or SLD). An interference pattern is generated by the combination (Figure 1-1A and 1-1B, interferometer) of backscattered light from the reference arm, which oscillates back and forth to provide depth information, and the sample arm.

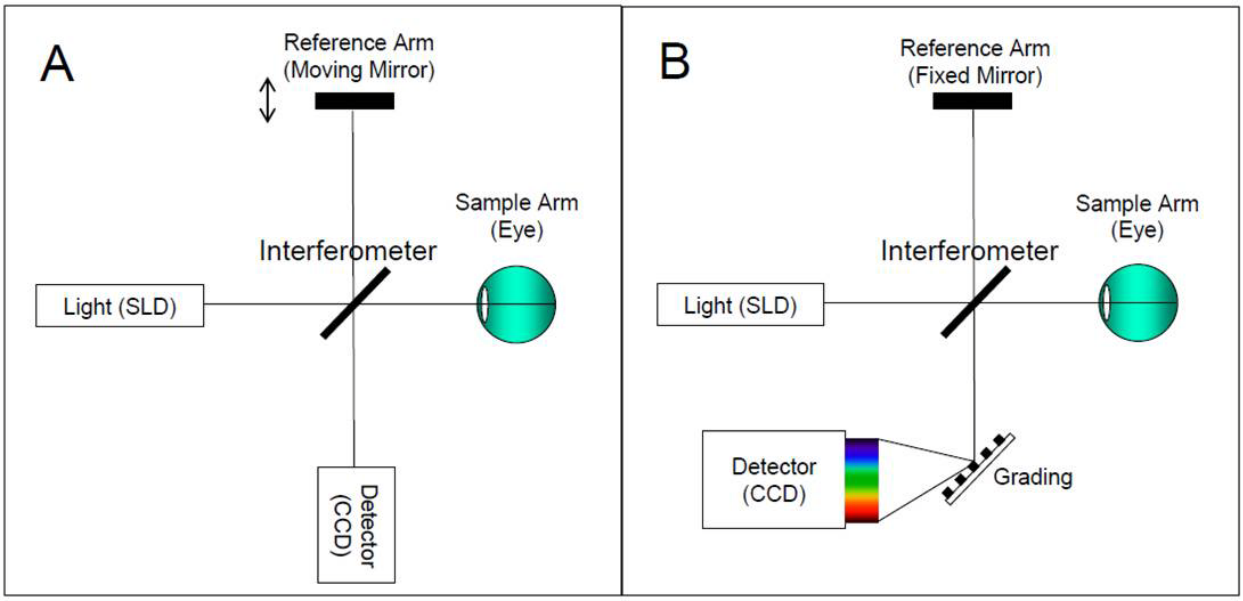

Figure 1-1. Diagrams of A) TD-OCT and B) SD-OCT.

The interference of two sources (i.e., reference and sample arms) can be described by the following equation:

$$I(\tau) = \frac{1}{2} \times (I_{ref} + I_{sam}) + Real[< E_{ref}(t+\tau) \times E_{sam}(t) >]$$

I: Intensity of light
I_{ref} : Intensity of the reference arm
I_{sam} : Intensity of the sample arm
$E_{ref}(t+\tau)$: Back-scattered light from the reference arm at time τ
$E_{sam}(t)$: Back-scattered light from the sample arm
$< E >$: Average over time
$I(\tau)$: Intensity of interference at time τ

Then, this interference pattern, $I(\tau)$, can be converted into a gray-scale image. The commercial TD-OCT system (StratusOCT, Carl Zeiss Meditec, Dublin, CA) optimized for ophthalmology use, has an axial resolution of 8-10μm and obtains B-mode scans at a rate of 400 A-scans per second. With OCT, various layer structures of the human retina can be analyzed qualitatively as well as quantitatively. [4-8]

Recently, more advanced OCT systems (spectral domain OCT or SD-OCT) have been introduced (Figure 1-1). SD-OCT has eliminated the necessity of mechanical motion in the reference arm by acquiring the entire axial samplings simultaneously in the frequency domain using a grating optics system, which resulted in a dramatic improvement in sampling speed. [2, 3] The interference pattern in frequency domain (Figure 1-1B, rainbow color) needs to be converted into time-domain to be visualized as a gray-scale image. The faster sampling of SD-OCT allows the acquisition of comprehensive, 3D volumetric information on the retina and optic nerve head. [9] Several SD-OCT instruments are commercially available, most operating with 5-7μm axial resolution at least 25,000 A-scans per second.

1.2 GLAUCOMA AND CLINICAL ASSESSMENT BY OCT

1.2.1 Glaucoma

Glaucoma is a slow progressive optic neuropathy, which induces irreversible structural damage (retinal ganglion cell (RGC) loss and retinal nerve fiber layer (RNFL) thinning) in the retina (Figure 1-2). [10-12] Glaucoma is also one of the leading causes of blindness not only in the United States but also globally. Glaucomatous damage can be triggered by many factors including intraocular pressure (IOP) and structural changes of the optic nerve head. [10-12]

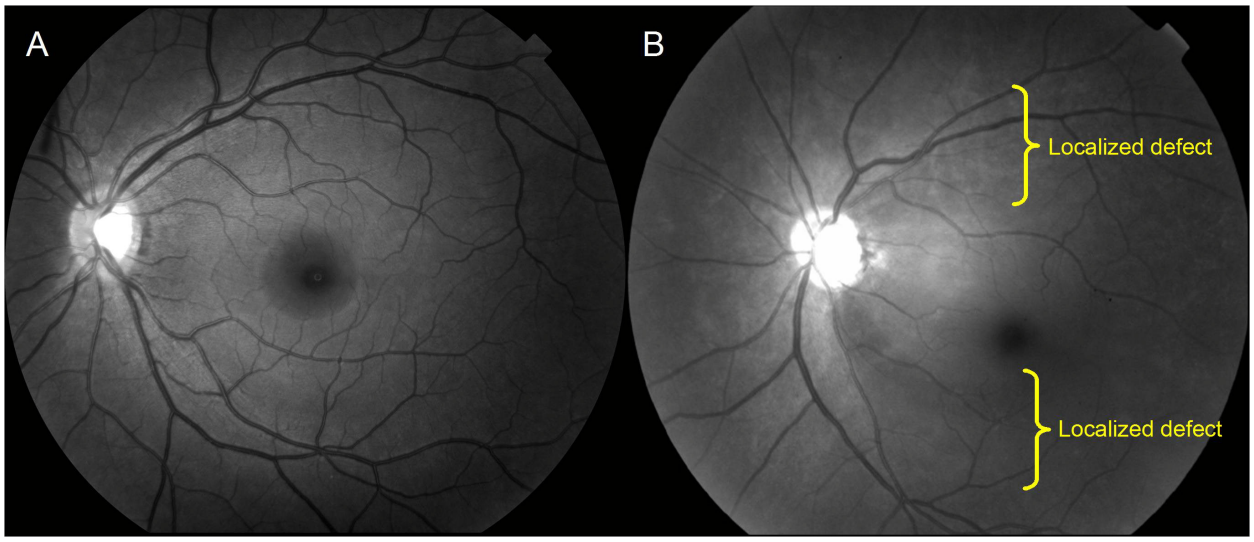

Figure 1-2. Localized glaucomatous damage appears on fundus photo: A) healthy eye and B) glaucoma eye. The localized defect region (B, shadowed region) resembles retinal axon bundle pattern because glaucomatous damage occurs along axon bundle.

1.2.2 Clinical assessment

There are two ways to detect glaucoma: 1) functional assessment and 2) structural assessment. Visual field (VF) testing has been long used as gold standard for assessing functional glaucomatous damage (Figure 1-3, upper). However, due to its subjective measurements, test-to-test variability is often substantially large. Moreover, by the time minimal VF abnormality appears, up to 40% of RNFL might have already been lost. [13-15] This is a critical limitation of this test because glaucomatous damage is irreversible. Early detection is essential for effective glaucoma treatment.

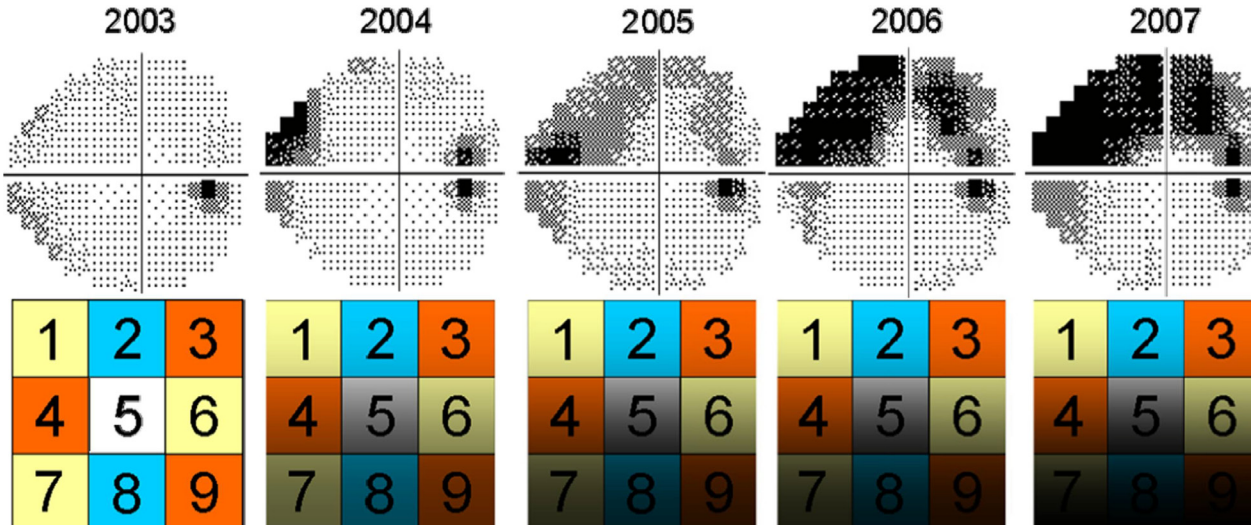

Figure 1-3. Glaucomatous damage sample: visual field tests (upper) in different time points and reconstruction of gradual vision loss from the same eye (lower). One third of the template image projected on the retina became dark (vision loss) at the year 2007 due to glaucomatous damage.

Structural damage can be assessed by many different imaging modalities such as traditional fundoscopy and color optic disc photography, and more recently confocal scanning laser ophthalmoscopy (CSLO), scanning laser polarimetry (SLP), and OCT. [13-15] Recent

development of these ocular imaging modalities helped transform structural assessment from a subjective and qualitative method to an objective and quantitative one. Many studies suggested that structural changes of RNFL and optic nerve head (ONH) are earlier indicators for glaucomatous abnormality that may precede the VF abnormality. [15] With TD-OCT, a 3.4 mm diameter circular scan centered at the ONH (Figure 1-4) is used to measure RNFL thickness as the circular scanning pattern captures all incoming nerve fibers to the optic nerve. [13, 16] Multiple repeated TD-OCT scans over time are needed to assess glaucoma progression. [15]

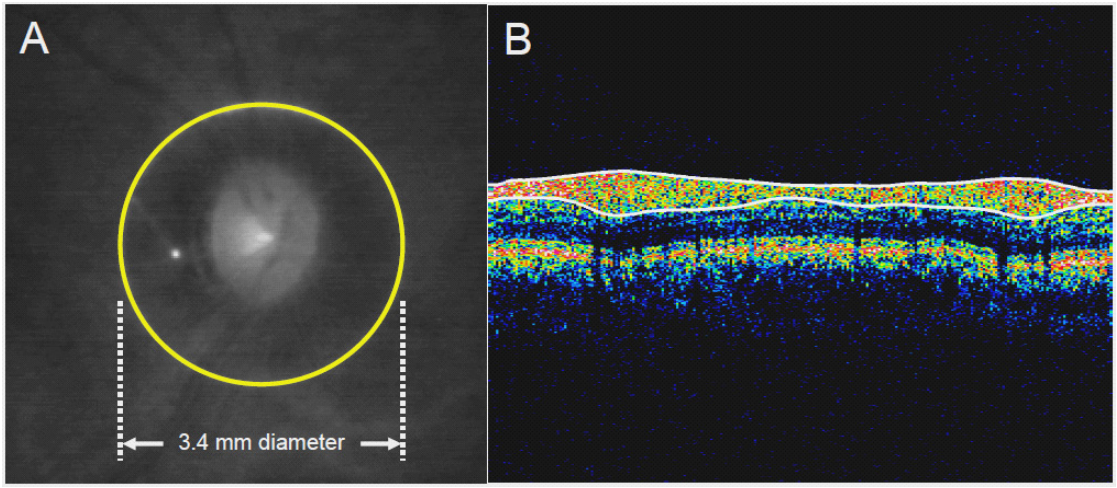

Figure 1-4. Visualization of A) TD-OCT 3.4 mm diameter circle scan (yellow) and B) its cross-sectional image and RNFL segmentation (white) along the yellow circle in depth. Major vessel generates a shadow artifact (vertical black lines on (B)) because scanning beam is absorbed by blood flow.

1.3 ANATOMY OF THE RETINA

Figure 1-5 shows the healthy human retina. The retina is a thin transparent layer and captures light like the charge-coupled device (CCD) camera (Figure 1-6, left). [10, 17, 18] The retina can be divided mainly into many different regions: periphery, macula and fovea. [10, 17, 18] Fovea

is a small round area in the center of the retina and has the highest visual acuity. The region around the fovea is called the macula, which is responsible for central vision. The ONH consists of a big bundle of retinal nerve fibers and blood vessels. Retinal nerve fibers (Figure 1-6 and 1-7) originate from the retinal ganglion cells, which receive visual information from photoreceptors and transmit visual information from the retina to the brain (i.e., visual cortex) through the ONH. [10, 17, 18] The cross-section of the retina is composed of many different cell layers (Figure 1-6, right). [10, 17, 18] The top highly reflective layer is called RNFL, and its thickness is considered as a clinically useful parameter in assessing glaucomatous damage. [10-13] Automated segmentation algorithms distinguishing the RNFL have been developed and are used widely for RNFL thickness measurements. [4-8]

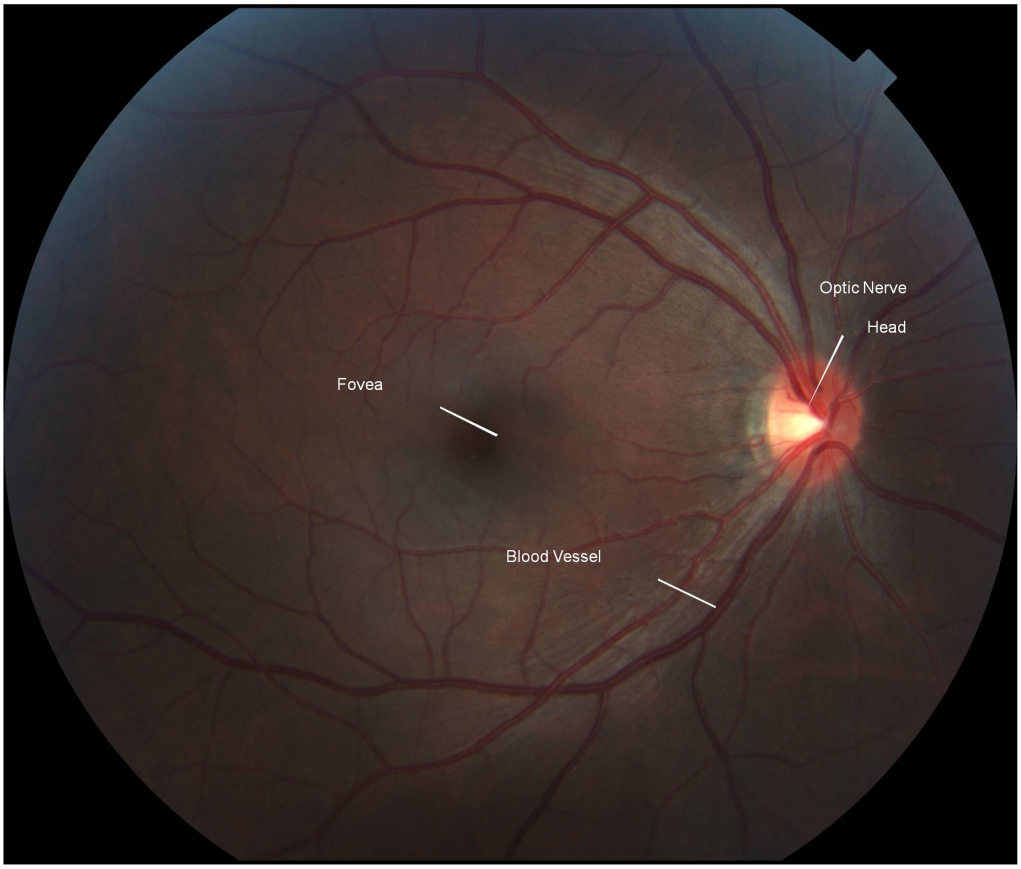

Figure 1-5. Appearance of the human retina.

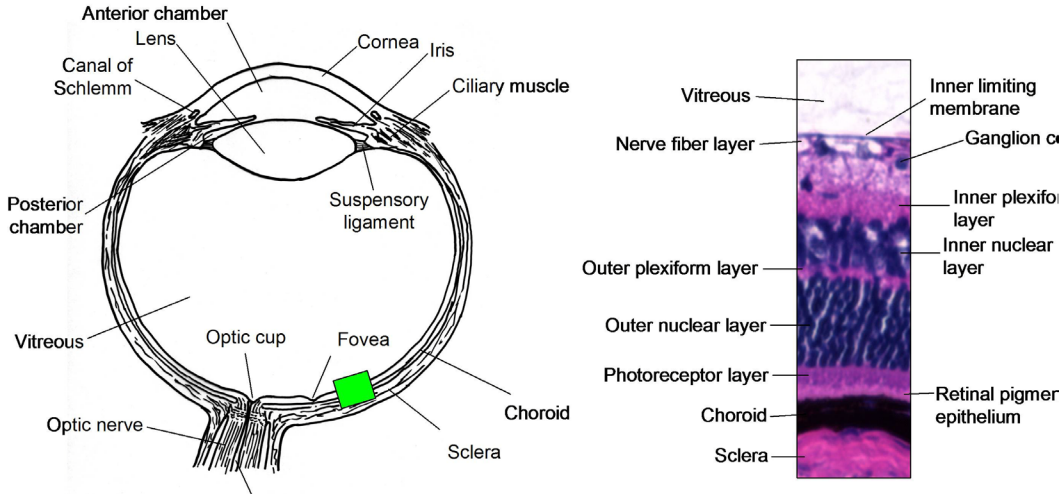

Figure 1-6. Anatomy of the human retina. The green colored region on left-hand side image is similar to the right-hand side image.

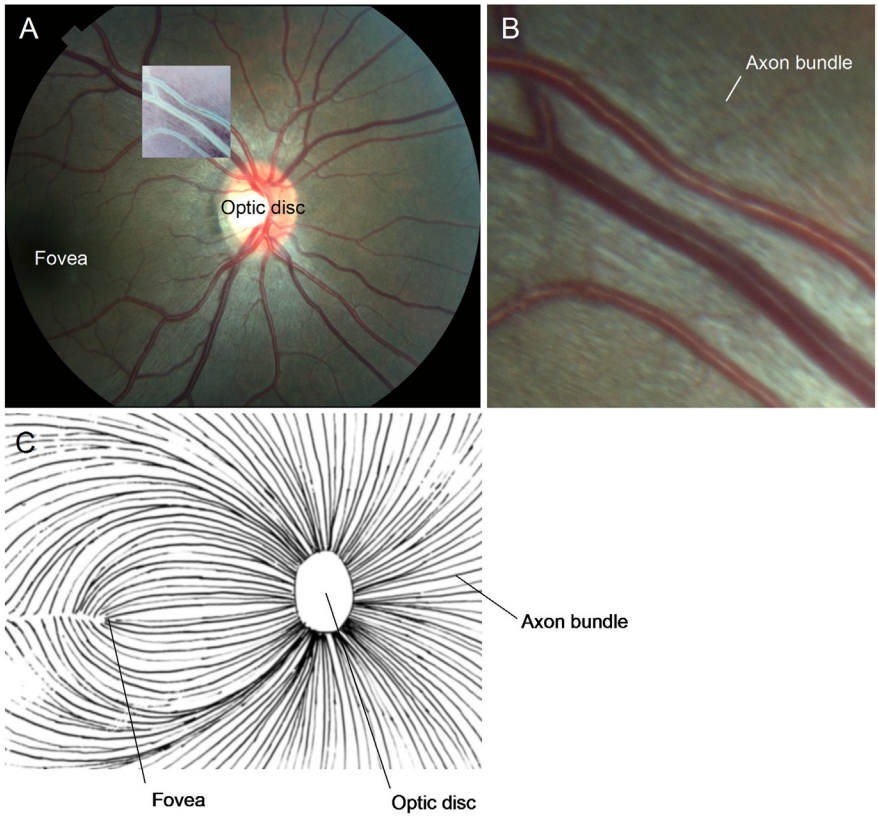

Figure 1-7. Axon bundle distribution pattern: A) Fundus photo, B) magnification of the inverted region on (A), and C) artistic drawing of axon bundle distribution on the retina.

1.4 CLINICAL PROBLEMS TO BE SOLVED

The above mentioned TD-OCT circular scan pattern (Figure 4-1) has certain limitations, which can induce significant RNFL thickness measurement variability (Figure 1-8). [19-21] First, scan location varies from scan to scan due to manual placement of the scanning circle position (operators manually center the scan circle on the ONH) (Figure 1-8A). Secondly, sampling points can be scattered along 3.4mm diameter circle due to eye motion during relatively slow scanning of TD-OCT (Figure 1-8B).

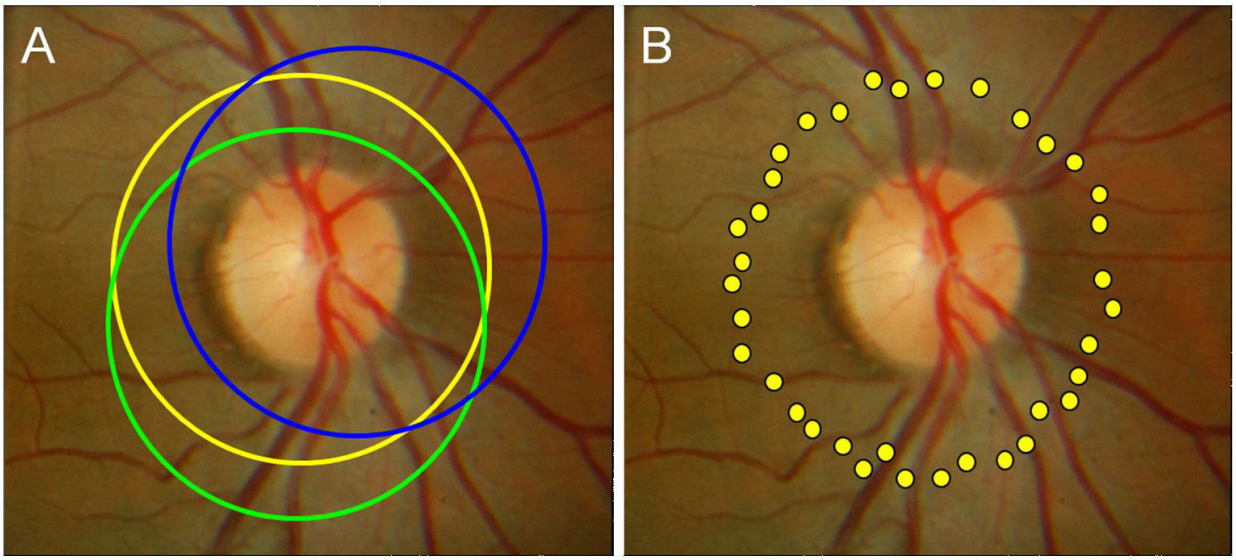

Figure 1-8. Major sources of retinal nerve fiber layer thickness measurement variability using 3.4 mm circular OCT scan centered on the optic nerve head. A) Scanning circle placement may vary from scan to scan (yellow, green, and blue circles). B) Schematic presentation of sampling points scattered along 3.4mm diameter circle due to eye motion during the scan.

In addition, technological transition from TD- to has introduced backward data comparability problems between the two different OCT technologies. [22-24] The systematic measurement bias and variable segmentation algorithm behaviors due to different signal

characteristics between TD- and SD-OCTs make it impossible to directly compare the RNFL thickness data obtained from different OCT technologies. Lack of effective and practical data comparability forces physicians to retake the baseline measurements using newer technologies, which wastes all the accumulated measurements and shortens the longitudinal observation time. This is a critical limitation especially for glaucoma as it commonly appears with a slow progression rate. [22-24]

We hypothesize that both the backward comparability and scan/sampling location problems can be solved by utilizing the comprehensive 3D volumetric data obtained using SD-OCT. By summing all the axial reflectivity at each sampling point, a 3D data can be visualized as a 2D en face image (surface view) of the scanned retina (Figure 1-9). [9] On this view, one can design any virtual sampling path within the 3D data, which provides virtually perfect scan/sampling locations on every single 3D scan. Also one can detect the TD-OCT scan location within the corresponding SD-OCT 3D data by computing similarities between the original TD-OCT scan and a virtually resampled SD-OCT scan. With this matched scan location information, one can establish a proper conversion equation in order to make TD- and SD-OCT RNFL thickness measurements directly comparable.

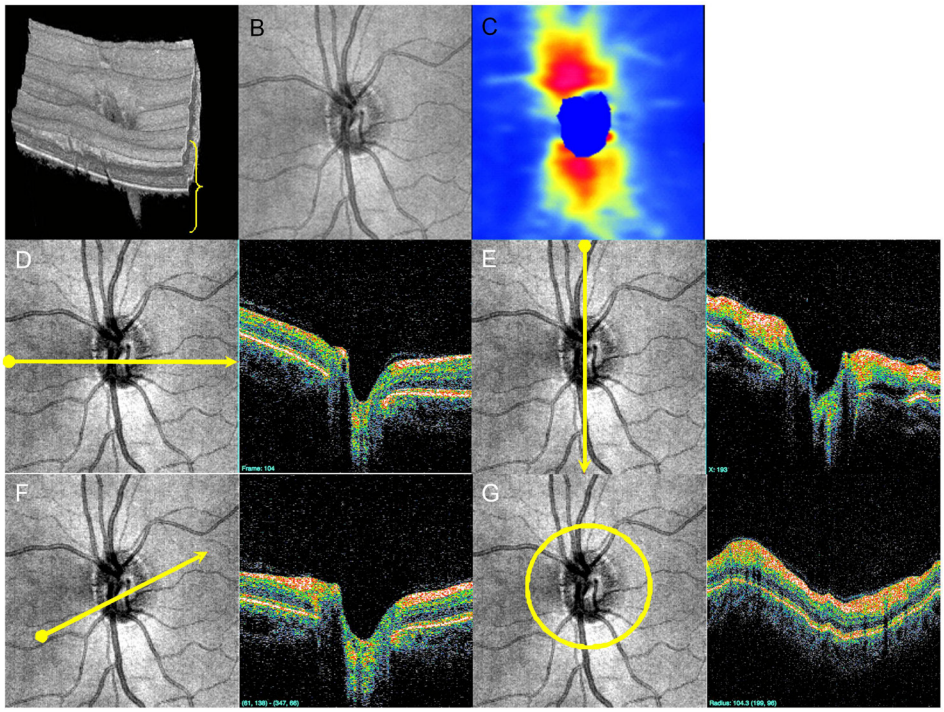

Figure 1-9. 3D SD-OCT data visualization: A) 3D SD-OCT volume rendered, B) OCT fundus image, C) 2D RNFL thickness map, D) horizontal re-sampling, E) vertical re-sampling, F) arbitrary angle re-sampling, G) circular re-sampling. By summing the reflectivity data in z-direction (A), OCT fundus (en face) image is generated (B). On the OCT fundus image, one can specify any re-sampling path (e.g., circular scanning path shown on G left) so that virtual re-sampled OCT cross-sectional image can be generated (G right).

1.5 PROJECT OBJECTIVES

The overall goal of this project is to improve the clinical utility of OCT RNFL measurement by establishing data comparability across the OCT technology generations and models. To achieve this, first, we developed a scan location matching (SLM) method (PCT/US2009/052951 pending) to find the matching center location of TD-OCT circular scan within 3D SD-OCT volume (Objective #1). [25] Next, we tested the SLM method with multiple SD-OCT devices for assessing its robustness since different SD-OCT devices use different 3D data scanning patterns;

one is spatially isotropic (evenly spaced) and others are anisotropic (oddly spaced) (Objective #2). With the Objectives #1 and 2, the above raised clinical problems are mostly solved except for progression trend analysis. By making TD-OCT measurement in one time point comparable to the most recent SD-OCT measurement, glaucoma progression can be assessed between one time point in the past and the present time. However, due to the variable TD-OCT scan locations in multiple visits in the past, still one cannot analyze the trend of glaucoma progression as RNFL thickness measured at different locations are not directly comparable. Therefore, we developed a mathematical model of the retinal nerve fiber bundle distribution (RNFBD) pattern to normalize the RNFL thickness measurements of off-centered TD-OCT circle scans to a virtual universal location centered on the ONH (Objective #3). Both the mathematical model of the RNFBD pattern and the SLM algorithm [25] were used for RNFL thickness normalization. The outcome of this study would facilitate more accurate and reliable glaucoma disease/progression detection in cross-sectional as well as longitudinal clinical settings.

1.5.1 Objective 1: Development of scan location matching (SLM) method, which finds the TD-OCT circle scan location within 3D SD-OCT volume

With the conventional TD-OCT, RNFL thickness is measured on a cross-sectional retinal image sampled along a 3.4mm circle centered to ONH. [13, 16] Due to the operator dependent nature of OCT scan registration, one of the major causes of measurement variability is inconsistent scanning circle placement, which may affect the accuracy and reliability of long term follow-up using TD-OCT (Figure 1-8A). SD-OCT can be used to obtain a raster scan to acquire a 3D volumetric data set within the same amount of scanning time as single TD-OCT imaging. SD-

OCT volume can be visualized as an en face image of the scanned area on the retina (OCT fundus image) by the backscattered signal at each transverse point on the retina. [26, 27] The OCT fundus image allows us to detect eye motion during scanning by checking the retinal blood vessel integrity and to create a virtual OCT cross-sectional image along any sampling line (curved or straight; Figure 1-9). This virtual sampling capability minimizes the above mentioned scanning circle placement variability because the virtual sampling happens after image acquisition allowing near perfect circle placement. At the same time, if the scanning circle placement of the baseline scan is not well centered, the virtual sampling may allow us to match the scanning location with the off-centered baseline scan so that the RNFL thickness measurement can be directly compared.

The aim of this objective was to develop and implement an OCT SLM algorithm, which finds the original scan location of a TD-OCT cross-sectional image within the corresponding 3D SD-OCT volume. The performance of SLM algorithm was quantified by comparing the TD-OCT peripapillary scan center to the matched SD-OCT scan center. The absolute difference of RNFL thickness measurement was also compared.

1.5.2 Objective 2: The performance investigation of SLM method with various SD-OCT devices

SD-OCT 3D volume scan, which is a series of multiple horizontal cross-sectional images (B-scans) scanned in a raster fashion, is a common scanning protocol with SD-OCT. However, 3D SD-OCT volume samples can be spatially isotropic (spatially evenly sized and spaced) or anisotropic (spatially oddly sized and spaced) depending on the makes and models of SD-OCT. It is possible that this spatial sampling variation may affect the performance of SLM method

because SLM is based on the similarity of the measurement between two different scans. For example, when SD-OCT volume contains a relatively smaller number of samples in one axis than the other, its similarity to TD-OCT scan, which is evenly sampled along a circle, may decrease along a lesser sampled axis resulting in larger SLM error or vice versa.

Therefore, the second aim of this project was to compare the performance of SLM method on multiple commercial SD-OCT devices that provides spatially isotropic and anisotropic volumes: Cirrus HD-OCT (spatially isotropic, 200x200 samplings in 6x6 mm), RTVue (spatially anisotropic, 513x101 samplings in 4x4 mm; Optovue, Fremont, CA), and Spectralis (spatially anisotropic, 512x193 samplings in 6x6 mm; Heidelberg Engineering, Heidelberg, Germany). Moreover, not only the scanning protocol but also the signal characteristics are different among these units.

In this objective, the performance of SLM method was quantified by comparing TD-OCT peripapillary scan center to matched SD-OCT scan center. In addition, the calibration equation between TD- and SD-OCT devices (Cirrus, RTVue, and Spectralis) was also computed.

1.5.3 Objective 3: Virtual normalization of TD-OCT circular scan locations

We have established a method to make TD-OCT RNFL thickness measurements in one time point directly comparable to the corresponding SD-OCT RNFL thickness measurements in another time point. Hence, longitudinal TD-OCT data can be compared to the present SD-OCT data, without requiring multiple time points where both scans are acquired, for trend analysis. Scan-to-scan RNFL thickness measurement variability is relatively high mainly due to the operator dependent manual placement of the TD-OCT circular scanning path (variable TD-OCT

circular scan locations). This prevents us to compare multiple time points together even after scan location matching and proper measurement conversion (both fixed and variable bias).

Retinal nerve fiber bundles form a pattern specific to each individual. A pattern can be generated from a 2D RNFL thickness map of a given SD-OCT 3D data. By mathematically modeling the pattern, virtual RNFL thickness values can be computed on any sampling circle location based on the actual values measured on one location. In other words, RNFL thickness measured along an off-centered circle can be normalized to the RNFL thickness virtually sampled along the properly centered circle. This way, multiple TD-OCT RNFL thickness measurements at multiple visits can be made comparable to each other even when the actual scan locations vary.

The aim of this final objective was to develop a mathematical model of the retinal nerve fiber bundle distribution (RNFBD) pattern to normalize the RNFL thickness measurements of off-centered TD-OCT circle scans to a virtual universal location properly centered on the ONH. The reproducibility of normalized RNFL thickness measurement was compared to the one from the actual TD-OCT circular scans (variable scan locations) in order to assess the clinical usefulness of this approach.

2.0 RETINAL NERVE FIBER LAYER THICKNESS MEASUREMENT COMPARABILITY BETWEEN TIME DOMAIN OPTICAL COHERENCE TOMOGRAPHY (TD-OCT) AND SPECTRAL DOMAIN OCT (SD-OCT)

SD-OCT is quickly replacing the conventional TD-OCT. SD-OCT allows a raster scan to acquire a 3D volumetric data set within the same amount of scanning time as single TD-OCT imaging (Figure 1-9A). SD-OCT volume can be visualized as an en face image (Figure 1-9B) of the scanned area on the retina (OCT fundus image) by the backscattered signal at each transverse point on the retina. [26, 27] The OCT fundus image allows us to detect eye motion during scanning, by checking the retinal blood vessel integrity and to create a virtual OCT cross-sectional image along any sampling line (curved or straight; Figure 1-9). This virtual sampling capability minimizes the above mentioned TD-OCT scanning circle placement variability because the virtual sampling happens after image acquisition allowing near perfect circle placement. At the same time, if the scanning circle placement of the baseline scan is not well centered, the virtual sampling may allow us to match the scanning location with the off-centered baseline scan so that the RNFL thickness measurement can be directly compared.

It is possible that SD-OCT may improve the sensitivity of glaucoma progression detection. [1, 28-30] However, SD-OCT RNFL thickness measurement is not directly inter-changeable with TD-OCT RNFL thickness measurement from the same eye. [22-24] Without ensuring the OCT measurement "backward-comparability", physicians must retake the baseline

measurements using newer technologies, which wastes all the accumulated measurements and shortens the longitudinal observation time. This is a critical limitation especially for glaucoma as it consists of a slow progression rate. [10-12] To our knowledge, there exists no method providing data comparability between TD- and SD-OCT.

We hypothesized that an automated detection of the TD-OCT circular scan registration location within the corresponding 3D SD-OCT can be achieved by utilizing OCT image data without using any external reference information, such as the TD-OCT video fundus image. The purpose of this study was to develop an automated system for such scan location matching between TD- and SD-OCT and to test its performance in terms of accuracy of the matched scanning circle location as well as the RNFL thickness measurements.

2.1 METHODS

Eleven eyes of 11 healthy subjects and seven eyes of seven glaucoma subjects from the University of Pittsburgh Medical Center Eye Center were enrolled. University of Pittsburgh Institutional Review Board and ethics committee approval were obtained for the study, and informed consent was obtained from all subjects. This study followed the tenets of the Declaration of Helsinki and was conducted in compliance with the Health Insurance Portability and Accountability Act.

2.1.1 Clinical diagnosis

Inclusion criteria were best corrected visual acuity of 20/40 or better, refractive error within ± 6.0 D, and no media opacities which interfere with fundus imaging. Subjects were excluded if they were using medications known to affect retinal thickness or if they had systemic diseases that might affect the retina or visual field. Subjects were also excluded if they had any previous intra-ocular surgeries other than uneventful cataract extraction. One randomly selected eye was included if both eyes were eligible in the same subject.

Healthy eyes had normal comprehensive ocular examination and automated perimetry glaucoma hemifield test (GHT) within normal limits (Humphrey Visual Field Analyzer, HVF IIi, Carl Zeiss Meditec, Inc. (CZMI), Dublin, CA). Glaucomatous eyes showed both glaucomatous optic neuropathy and GHT outside normal limits. Glaucomatous optic neuropathy was defined as general or focal neuro-retinal rim thinning, disc hemorrhage or inter-eye cup/disc (C/D) ratio asymmetry >0.2.

2.1.2 Image acquisition

The peripapillary region was scanned on all eyes using conventional TD-OCT (Stratus OCT; CZMI) and SD-OCT (Cirrus HD-OCT; CZMI) at a single visit. All scans were performed through dilated pupils.

2.1.2.1 TD-OCT

Circular scans centered on the ONH were obtained using the "Circle Scan" pattern, which was a single 3.4 mm diameter circular scan with 256x1024 samplings acquired in 0.64 second. Nine

Circle scans were obtained from each eye in a single session by one operator. Each of nine scans had its scanning circle manually centered differently (Figure 2-1). Starting with the circle manually centered on the ONH followed by eight different manual displacements so that each circle had clearly visible displacement without touching the ONH margin. Images with signal strength (SS) less than six were discarded as poor quality images as the manufacturer recommends. RNFL thickness was measured using the Stratus OCT system software version 5.0. Segmentation failure was defined as obvious deviation of the segmented inner and/or outer RNFL borders from the subjectively perceived borders. Consecutive 5% or cumulative 10% segmentation failure within a given image was considered to be poor analysis quality and discarded.

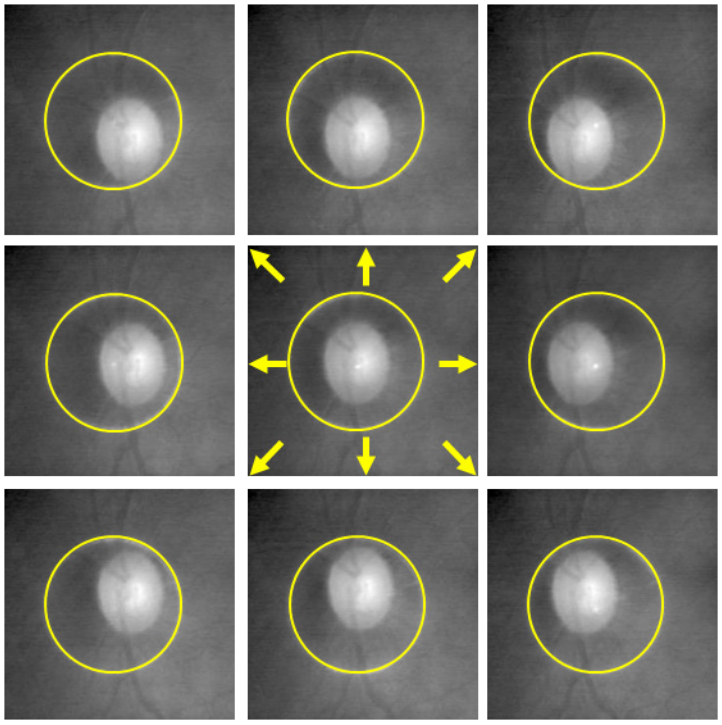

Figure 2-1. Illustration of TD-OCT Circle scans in 9 different locations per eye.

2.1.2.2 SD-OCT

A single Cirrus HD-OCT "Optic Disc Cube 200x200" scan was obtained from each eye. This isotropic (equal A-scan spacing in x, y plane) raster scan contained 200x200x1024 samplings of a 6x6x2 mm volume manually centered on the ONH, and was acquired in 1.48 seconds. Images with SS less than eight were discarded as poor quality images, as the manufacturer recommends. This cut-off differs from that of TD-OCT because of inherent hardware and software differences between the two platforms. Inclusion also required that eye movements be less than the diameter of major vessels judged on OCT fundus images. The segmentation quality criteria for virtual OCT slices (or re-sampled images) from the Cirrus scans was the same as for the Stratus OCT scans with the additional criteria of more than 10% of frames labeled as analysis failure disqualified any scan.

2.1.3 Scan location matching process

Every possible 3.4mm circular re-sampling paths contained within physical boundaries of the 3D SD-OCT scan was generated (Figure 2-2 and 2-3). Along each circle, a virtual OCT cross-sectional image was re-sampled with 256 evenly distributed sampling points (A-scans). The spatially closest actual A-scan data within the 3D volume were used for re-sampling arbitrary virtual location.

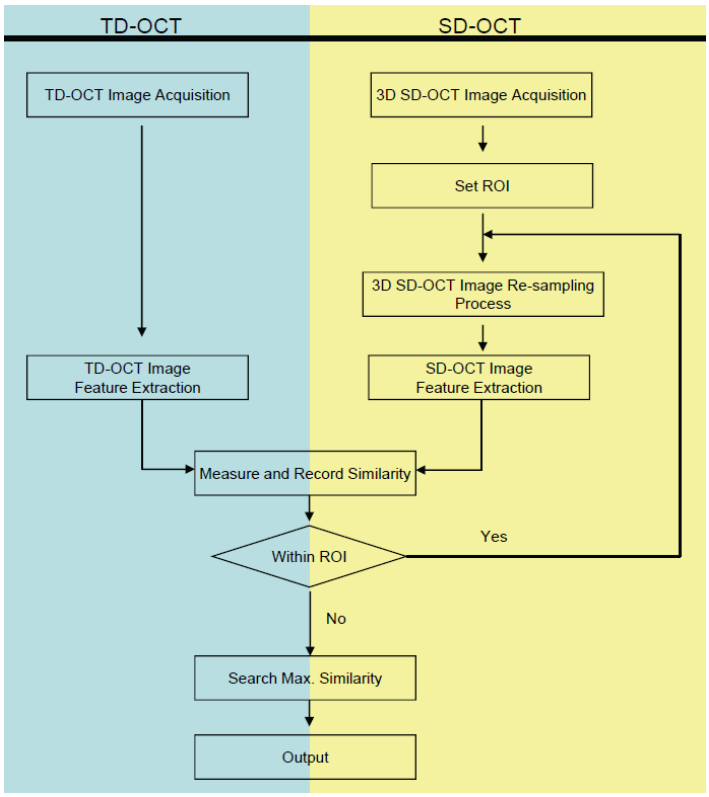

Figure 2-2. Diagram of scan location matching process.

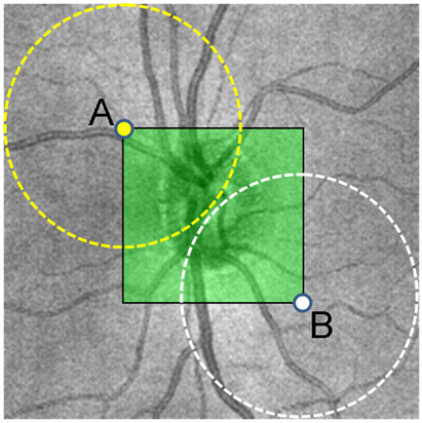

Figure 2-3. Visualization of re-sampling process boundary (region of interest). Re-sampling center boundary (light green square) was determined so that virtual 3.4 mm diameter circles did not go out of the sampled volume in order to avoid missing data point. During the search of the matching re-sampling center, the algorithm iterates from the center point A through the center point B pixel by pixel within the green square.

Each A-scan of the re-sampled scans was aligned to a corresponding A-scan in the TD-OCT circular scan. Similarity for each virtual scan was assessed by cross correlation, and a two-dimensional similarity map, with correlation coefficient value ranging from zero to one, was generated (Figure 2-4). .The location of the re-sampled scan with the highest correlation coefficient was automatically recorded as the most likely location of the center of the TD-OCT scan.

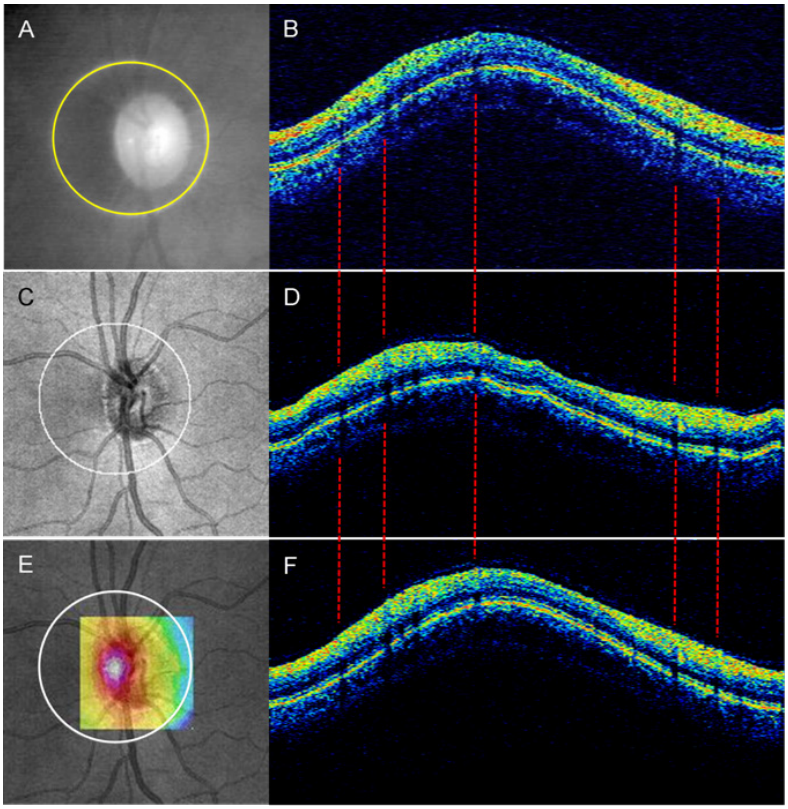

Figure 2-4. Scan location matching sample: A & B) Fundus video image (A) and cross-sectional OCT image (B) of a TD-OCT circular scan; C & D) OCT fundus image (C) and virtually re-sampled cross-sectional OCT image (D) of a SD-OCT 3D scan on the same eye; E) Similarity map was generated by computing correlation coefficients between TD-OCT data and virtually re-sampled data centered at each pixel within the re-samping center boundary (color ranges correlation coefficient 0 (dark blue) to 1 (white)); F) Aligned matching virtually re-sampled image (note the locations of the vessel shadows nicely match up with TD-OCT image; dashed lines).

2.1.4 Similarity assessment of the matched scan location

Agreement between matched scan locations was assessed by measuring the distance between the center points of the TD-OCT and the matched virtual SD-OCT scans. Global and sectoral RNFL thickness measurements from these two OCT scans were also compared.

2.1.4.1 Distance between the center points

Each TD-OCT video fundus image was manually registered with the corresponding SD-OCT fundus image by rotation, scaling, and translation, using major vessels as references (Figure 2-5). The distance between the center points of the scan circles was measured on the composite image.

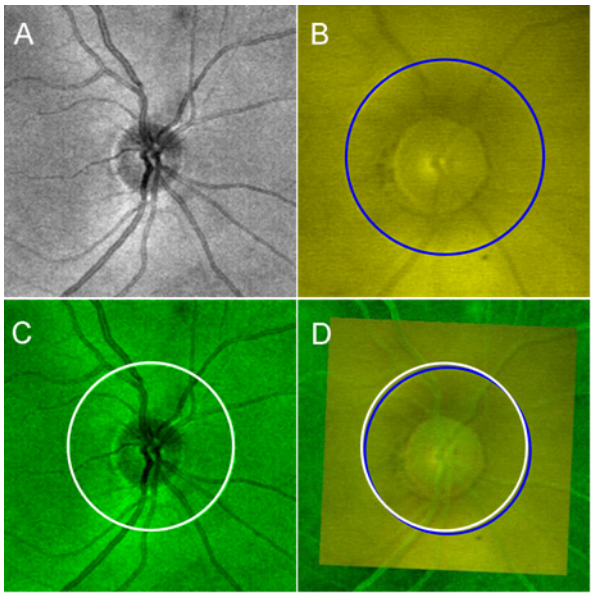

Figure 2-5. Manual registration of TD-OCT video fundus image with SD-OCT fundus image: A) SD-OCT fundus image; B) TD-OCT video fundus image with circle scan location (blue); C) matched scan location with virtual 3.4 mm circle on SD-OCT fundus image; D) two fundus images manually registered by rotating, scaling, and translation (green SD-OCT fundus image superimposed on TD-OCT video fundus image (yellow)) and matched scan circle (white) was imported to the registered image.

2.1.4.2 RNFL thickness measurements comparison

RNFL thickness, from the nine TD-OCT scans, was obtained using the Stratus OCT system software (version 5.0). SD-OCT RNFL thickness measurements were obtained using Cirrus HD-OCT the system software (version 3.0) at both the default ONH centered location and the matched scan location.

A calibration equation was computed to compensate for the systematic difference in RNFL thickness measurement between TD-OCT and SD-OCT. This computation was performed by using an independent group consisting of 48 eyes of 24 healthy subjects. All eyes satisfied the above criteria for healthy eyes and were scanned both with TD- and SD-OCT at the same visit. The details of the calibration equation computation are described in the appendix A.

2.1.5 Statistical Analysis

A mixed effect model [31-33] was used to estimate the difference between the TD-OCT scan location and the matched scan location on the SD-OCT 3D volume. In addition, a structural equation model (SEM; Figure 2-6) was used to model the measurement error of the devices. This model describes the relative systematic error (bias) between devices and the random error (imprecision) of each device. Linear mixed effects model was used to compute the confidence intervals for the imprecision comparisons after calibration.

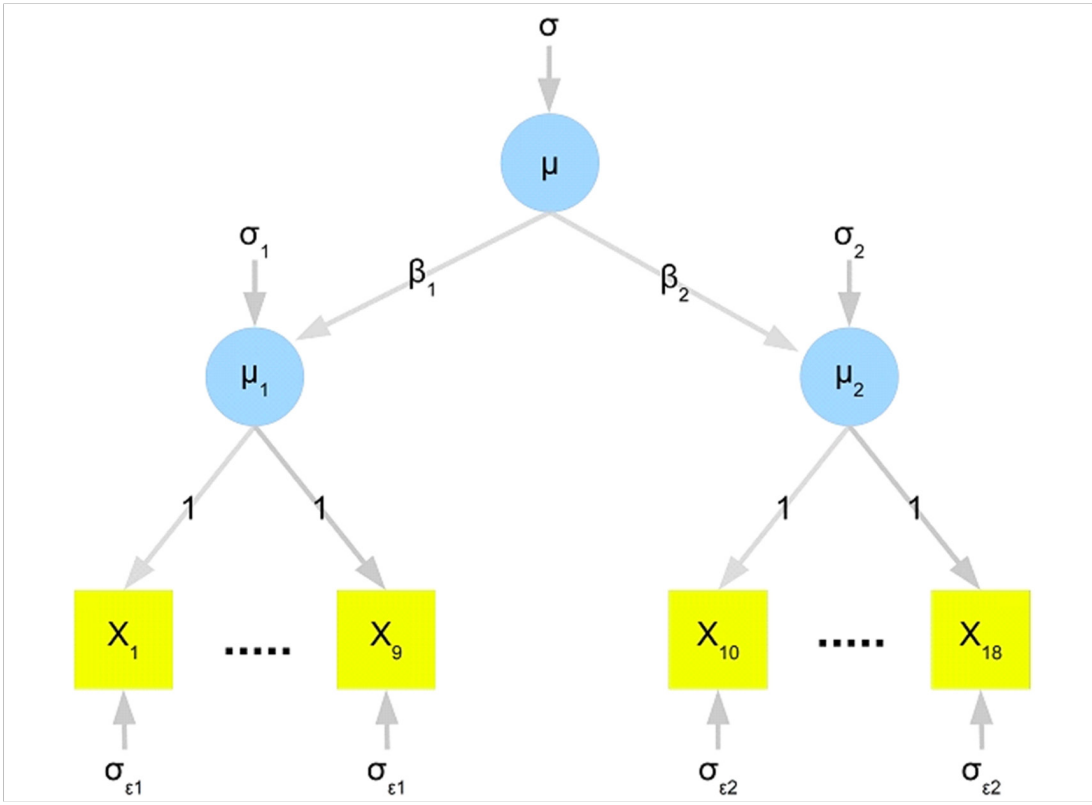

Figure 2-6. Diagram of structural equation model.

2.2 RESULTS

Subject demographics were summarized in Table 2-1. Healthy eyes had thicker mean RNFL thickness than glaucomatous eyes ($p<0.01$, mixed effects model).

Table 2-1. Subject demographics (mean ± standard deviation)

	Healthy (N=11)	Glaucoma (N=7)
Male : Female	5 : 6	2 : 5
Age (years)	37.6 ± 10.6	63.2 ± 4.3
TD-OCT RNFL Thickness (μm)	112.2 ± 11.7	88.6 ± 16.5

2.2.1 Distance between the center points

The distance between TD-OCT scan circle centers and the corresponding matched virtual SD-OCT scan circle centers were 2.3 pixels (69.0 μm on the retina) for healthy eyes and 3.1 pixels (93.0 μm on the retina) for glaucomatous eyes (Table 2-2). These distances were notably smaller than the distance (e.g., 15.1 [14.3 – 15.8] pixels of mean displacement, $p<0.01$) between the matched scan location and the properly centered scan location on a given SD-OCT 3D volume data (Figure 2-7). When the matched distance was decomposed into X and Y components, there was no statistically significant difference between the two components for both healthy and glaucomatous eyes.

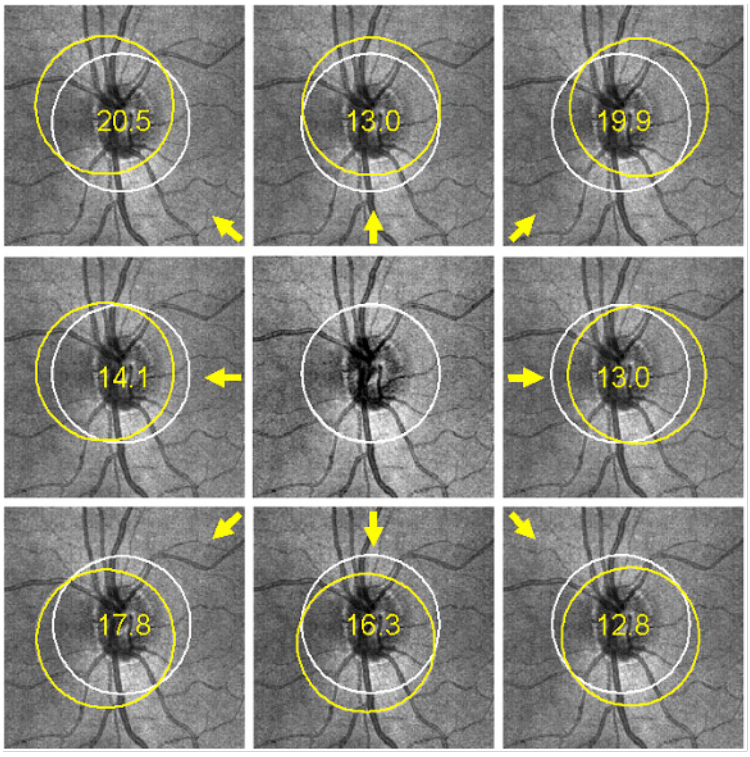

Figure 2-7. A sample case for distances (in pixels) between matched circle (yellow) and the properly centered circle (white) on SD-OCT fundus image.

Table 2-2. Distance between scanning circle center points (mean [95% confidence interval])

Distance	Healthy		Glaucoma	
	Pixel	Distance on Retina (μm)	Pixel	Distance on Retina (μm)
Center Distance	2.3 [1.5 – 3.2]	69.0 [45.0 – 96.0]	3.1 [2.0 – 4.1]	93.0 [60.0 – 123.0]
X Component of Distance	1.6 [0.7 – 2.4]	48.0 [21.0 – 72.0]	1.9 [0.8 – 2.9]	57.0 [24.0 – 87.0]
Y Component of Distance	1.3 [0.7 – 2.0]	39.0 [21.0 – 60.0]	2.0 [1.2 – 2.8]	60.0 [36.0 – 84.0]

2.2.2 RNFL thickness measurements comparison with and without scan location matching

Table 2-3 shows the RNFL measurements in four conditions for each of healthy and glaucomatous eyes. The difference between TD- and SD-OCT measurements with and without scan location matching was summarized in Table 2-4. Diagnosis statistically significant influenced measurement differences in 4 sectors (temporal quadrant and clock hours 8, 9, 10, and 12; Table 2-5). The RNFL measurement differences were statistically significantly smaller with scan location matching than without in all sectors except for clock hours 8, 9, and 10 for glaucomatous eyes.

Table 2-3. Retinal nerve fiber layer thickness results (μm) on time domain OCT (TD-OCT; with and without calibration) and spectral domain OCT (SD-OCT; with and without scan location matching).

Sector		Healthy				Glaucoma			
		TD-OCT	TD-OCT Calibrated	SD-OCT No Matching	SD-OCT Matched	TD-OCT	TD-OCT Calibrated	SD-OCT No Matching	SD-OCT Matched
Global Mean		112.2	106.2	96.7	97.5	88.6	82.8	84.1	83.4
Quadrant	Temporal	84.5	74.0	64.7	73.9	78.3	69.1	65.1	70.9
	Superior	139.6	132.5	123.5	125.1	103.5	97.4	99.0	99.4
	Nasal	87.6	82.7	68.1	68.2	70.4	63.7	69.7	68.1
	Inferior	137.0	135.9	130.4	122.9	102.1	94.7	102.4	94.9
Clock Hour	1	128.7	115.3	116.6	115.1	92.1	90.4	83.6	86.4
	2	100.2	97.0	88.1	84.2	79.0	73.1	83.1	79.3
	3	71.6	64.5	51.7	54.1	62.6	57.1	59.1	59.3
	4	91.0	82.6	64.5	66.3	69.7	61.0	66.9	65.7
	5	120.1	117.1	105.6	99.0	85.5	75.6	83.0	77.8
	6	143.1	143.5	140.0	128.7	108.4	101.5	111.9	100.2
	7	147.7	139.5	145.5	141.0	112.4	110.3	112.1	106.9
	8	89.0	78.6	65.9	80.4	80.0	71.0	63.9	76.8
	9	65.2	56.5	51.2	56.7	62.4	54.8	53.3	57.5
	10	99.5	92.9	77.2	84.7	92.7	85.5	78.0	78.6
	11	148.8	139.9	137.8	134.5	119.1	111.4	119.0	113.2
	12	141.2	140.6	116.3	125.7	99.1	89.5	94.3	98.5

Table 2-4. Retinal nerve fiber layer thickness absolute difference (μm [95% confidence interval]) between time domain OCT (TD-OCT) and spectral domain OCT (SD-OCT) comparison. Temporal quadrant and clock hours 8, 9, 10, and 12 were analyzed separately (Table 2-5).

Sector		Difference without Matching (A)	Difference with Matching (B)	A-B	p-value
Global Mean		10.1 [7.0 − 13.2]	9.1 [6.1 − 12.2]	1.0	0.02
Quad-rant	Superior	16.6 [13.0 − 20.3]	10.3 [7.1 − 13.6]	6.3	<0.01
	Nasal	23.2 [19.3 − 27.1]	15.6 [12.2 – 19.0]	7.6	<0.01
	Inferior	20.0 [15.3 − 24.8]	13.9 [9.5 − 18.2]	6.2	<0.01
Clock Hour	1	15.1 [9.8 − 20.3]	11.1 [6.0 − 16.2]	4.0	<0.01
	2	25.6 [21.6 − 29.7]	16.9 [13.5 − 20.4]	8.7	<0.01
	3	16.6 [13.1 − 20.1]	11.9 [8.7 − 15.1]	4.7	<0.01
	4	24.4 [18.8 − 29.9]	17.6 [12.4 − 22.7]	6.8	<0.01
	5	28.8 [23.1 − 34.5]	18.9 [14.4 − 23.4]	9.9	<0.01
	6	30.3 [25.1 − 35.6]	17.6 [13.3 − 21.9]	12.7	<0.01
	7	19.0 [15.3 − 22.6]	11.9 [8.8 – 15.0]	7.1	<0.01
	11	19.4 [16.1 − 22.7]	11.9 [9.1 − 14.7]	7.5	<0.01

Table 2-5. Retinal nerve fiber layer thickness absolute difference (μm [95% confidence interval]) between time domain OCT (TD-OCT) and spectral domain OCT (SD-OCT) comparison at the sectors that showed statistically significant interaction between methods (with and without scan location matching) and diagnosis (healthy and glaucoma).

Sector	Healthy				Glaucoma			
	Difference without Matching (A)	Difference with Matching (B)	A-B	p-value	Difference without Matching (C)	Difference with Matching (D)	C-D	p-value
Temporal	14.3 [11.6 – 16.9]	4.6 [3.4 – 5.8]	9.7	<0.01	11.3 [9.4 – 13.3]	6.5 [13.3 – 8.3]	2.9	0.03
8	19.4 [15.2 – 23.5]	7.4 [4.6 – 10.1]	12.0	<0.01	14.7 [9.5 – 19.9]	6.5 [19.9 – 11.5]	3.0	0.12
9	9.1 [7.6 – 10.6]	4.6 [3.9 – 5.3]	4.4	<0.01	9.2 [7.1 – 11.4]	6.2 [11.4 – 9.0]	0.8	0.89
10	24.5 [18.6 – 30.4]	11.4 [6.8 – 15.9]	13.2	<0.01	21.2 [14.2 – 28.2]	9.4 [28.2 – 16.2]	4.8	0.06
12	37.9 [30.2 – 45.6]	18.4 [12.7 – 24.0]	19.5	<0.01	27.7 [22.2 – 33.3]	15.3 [33.3 – 20.0]	6.8	<0.01

2.3 DISCUSSION

We have invented and evaluated a method to simultaneously compensate both systematic measurement difference between TD- and SD-OCT and scan location variability associated with TD-OCT. The results suggest that our scan location matching algorithm properly identified the actual TD-OCT scan location within the corresponding 3D SD-OCT volume data with relatively small error. This allowed the comparison of RNFL measurements in essentially the same location between TD- and SD-OCT scans, improving agreement and reducing measurement variability.

Despite the relatively small sample size, RNFL thickness measurement differences between TD- and SD-OCT in most of the sectors were smaller with than without scan location matching, suggesting the robustness of the proposed algorithm. In most sectors, the measurement differences between TD-OCT and scan location matched SD-OCT were larger than the expected measurement errors on both TD- and SD-OCT. Since calibration adjustment removed the systematic measurement difference and the scan location matching algorithm removed the global registration components of measurement variability, the remaining differences may be attributed to A-scan location jitter due to eye movement during scanning (Figure 1-8B). The proposed algorithm re-samples data along a perfect circle, which precludes simulating the sampling jitter. Theoretically, the algorithm can be designed to look for the best match at every sampling location within the certain range based on the eye movement model. However, this approach will be computationally intensive and was not included in this first generation algorithm. The processing time per image is currently approximately 60 minutes. This can be reduced by optimizing the range of search (e.g. removing any re-sampling path intercepting the ONH) and

the computational routine (e.g. taking advantage of the hardware vector processing acceleration available to the latest processors). Further investigation and optimization are warranted.

The advantage of the present approach is that it requires only OCT data. No external reference information (e.g. fundus image) is required; therefore, it is possible to apply the same method to other TD-OCT and SD-OCT devices. Since multiple SD-OCT systems have been commercially introduced, data comparability issue between the legacy TD-OCT data and the new SD-OCT data needs to be resolved. A bridging method is needed to ensure a smooth technological transition while maintaining the integrity of longitudinal comparisons essential to detecting disease progression. The proposed method is a strong candidate to bridge the gap between TD- and SD-OCT RNFL measurements. Further investigation of its application to different TD- and SD-OCT devices is needed.

A potential limitation of the proposed algorithm is its unselective use of OCT data. Since it is assessing the similarity of the OCT data, it might be more advantageous to selectively use stable structures that are unlikely affected by glaucomatous changes (e.g. retinal blood vessels). Unfortunately, the cumulative area of the major retinal blood vessels within a circular OCT scan cross-section is less than one fifth of the entire image. Our unpublished pilot data using only blood vessel information revealed that the selective approach was not robust. Unless significant global damage is inflicted within a short period of time, we hypothesize that area affected by glaucoma progression within a circular OCT cross-section is small enough not to adversely affect the algorithm performance. However, this hypothesis is yet to be tested.

Another limitation of this study was that the Stratus video fundus images were used to assess the accuracy of scan location matching. The scan circle appearing on the Stratus video fundus image does not always correspond exactly to its cross-sectional image due to eye

movement during scanning. [19] This might have affected the distance assessment between TD- and SD-OCT scan locations. However, by subjectively observing the major retinal blood vessel shadows in cross-sectional OCT images, there was no clearly noticeable disagreement between TD-OCT scan and the corresponding matched virtual SD-OCT scan. Nonetheless, this might add to the residual difference that was noted between TD- and matched SD-OCT.

In conclusion, our novel method of scan location matching may bridge the gap in RNFL thickness measurements between TD-OCT circular scan and 3D SD-OCT scan data, providing longitudinal comparability between TD- and SD-OCT measurements.

3.0 COMPARABILITY TEST BETWEEN TIME DOMAIN OPTICAL COHERENCE TOMOGRAPHY (TD-OCT) SCAN AND SPATIALLY ISOTROPIC/ANISOTROPIC THREE DIMENSIONAL (3D) SPECTRAL DOMAIN OCT (SD-OCT) SCAN

Our previous aim [25] demonstrated a novel method, which can be used to establish backward data comparability between two generations of OCT technologies, TD-OCT (Stratus OCT) and SD-OCT (Cirrus HD-OCT), by detecting TD-OCT scan location within 3D SD-OCT cube scan. However, there are many different SD-OCT devices providing various scan designs. For example, a 3D SD-OCT scan can be performed in two ways (Figure 3-1): spatially isotropic (evenly sampled) scan and anisotropic (unevenly sampled) scan. In the previous study, the performance of SLM algorithm was measured with spatially isotropic 3D SD-OCT cube scans (Cirrus HD-OCT Optic Disc Cube 200×200).

We hypothesized that SLM method is robust and can be applied to any 3D SD-OCT data regardless of scan design. However, it is possible that this spatial variation in scanning pattern may affect the performance of SLM method because SLM algorithm is based on the similarity measurement between two different scans (Figure 2-2, 2-3, and 2-4). For example, when the sampled points of SD-OCT, along the virtual 3.4 mm diameter circle, are less than the 256 points of the TD-OCT circle scan, a bigger SLM error will result. The purpose of this study was to compare the performance of the SLM method on SD-OCT devices that provide both spatially

isotropic and anisotropic volumes and to investigate the RNFL thickness measurement difference as well.

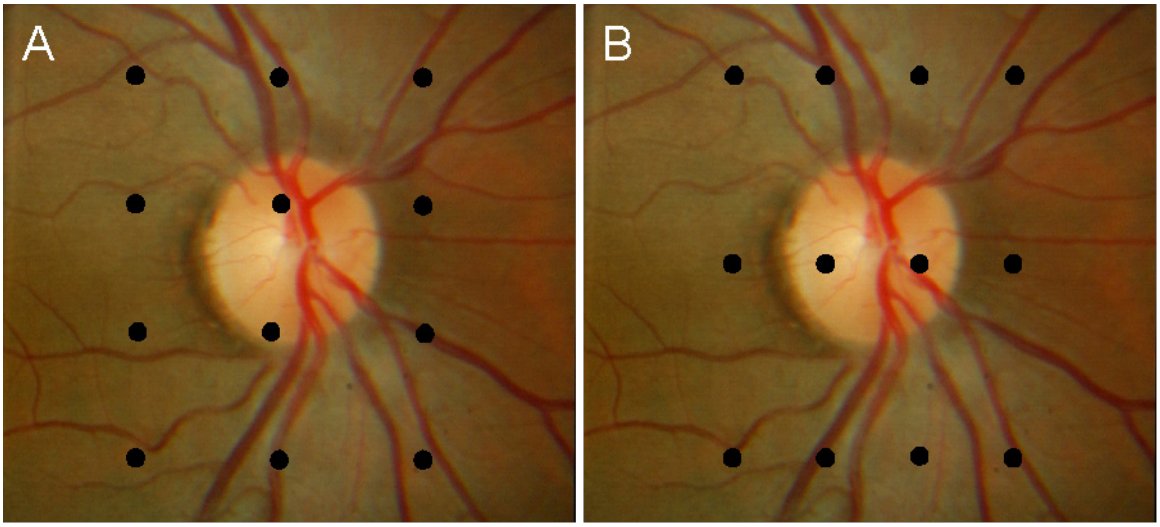

Figure 3-1. Illustration of spatially isotropic (A) and anisotropic (B) 3D SD-OCT volume scans. Each black dot represents single A-scan.

3.1 METHODS

Twelve eyes of 12 healthy subjects and seven eyes of seven glaucoma subjects from the University of Pittsburgh Medical Center Eye Center were enrolled. University of Pittsburgh Institutional Review Board and ethics committee approval were obtained for the study, and informed consent was obtained from all subjects. This study followed the tenets of the Declaration of Helsinki and was conducted in compliance with the Health Insurance Portability and Accountability Act.

3.1.1 Clinical diagnosis

Inclusion criteria were identical to the previous study design (section 2.1.1). Healthy and glaucoma eyes were defined by the previous study design (section 2.1.1), as well. The peripapillary region was scanned on all eyes using conventional TD-OCT (Stratus OCT) and SD-OCT (Cirrus, RTVue, and Spectralis) at the same visit. All scans were performed through dilated pupils.

3.1.2 Image Acquisition

3.1.2.1 TD-OCT

The image acquisition of the TD-OCT 3.4 mm diameter circle scan was identical to the previous study design (section 2.1.2.1). Nine circular scans were obtained from each eye in a single session by one operator. Each of nine scans had its scanning circle manually centered differently by moving the fixation target (Figure 2-1).

3.1.2.2 SD-OCT

Three SD-OCT volume scans per eye were obtained from three SD-OCT devices (one from each device): Cirrus HD-OCT Optic Disc Cube 200×200 (spatially isotropic, 200×200 samplings in 6×6 mm), RTVue 3D Disc (spatially anisotropic, 513×101 samplings in 4×4 mm), and Spectralis (spatially anisotropic, 512×193 samplings in 6×6 mm) (Table 3-1, Figure 3-2). Scans were included with signal strength (SS) scores recommended by manufacturer: SS scores of Cirrus, RTVue, and Spectralis were eight or above, 57 or above, and blue, respectively. Included scans also required that eye movements be less than the diameter of major vessels appeared on SD-

OCT fundus (*en face*) image. RNFL thickness was measured on every sampling point, except for the area within the ONH, in a fully automated fashion using a software program of our own design. The volume scans with more than 10% of frames labeled as RNFL analysis failure were considered as poor quality scans and discarded. The segmentation failure criteria for virtual OCT slices (or re-sampled images) from the SD-OCT scans was the same as for the TD-OCT scans.

Table 3-1. Specification of SD-OCT devices. The scanning time of Spectralis depends on the amount of eye motion during scanning because eye motion tracking is on.

		Cirrus	RTVue	Spectralis
Scan Type		Isotropic	Anisotropic	Anisotropic
SD-OCT window size	mm	6×6	4×4	6×6
	pixel	200 (W) × 200 (H)	513 (W) × 101 (H)	512 (W) × 193 (H)
Scanning speed (A-scans / sec)		27,027	52,000	40,000
Scanning time (sec.)		1.48	1.00	N/A

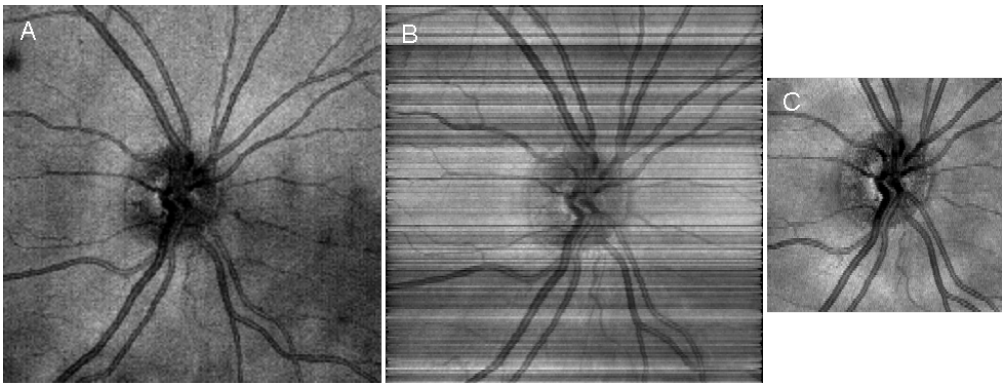

Figure 3-2. 3D SD-OCT volume scans from three different manufacturers: A) Cirrus HD-OCT Optic Disc Cube 200×200, B) Spectralis volume scan, C) RTVue 3D Disk.

3.1.3 Scan location matching (SLM) process

The scan location matching algorithm finds a TD-OCT scan within the SD-OCT volume scan by measuring the similarity between the two OCT cross-sectional images (Figure 2-3 and 2-4). [25] The detailed methodology is described in the previous aim, but briefly, every possible 3.4mm circular scan contained within the physical boundaries of the 3D SD-OCT scan was generated by mimicking the "Circle scan" pattern of conventional TD-OCT. The radius of the sampling circle was adjusted for each device according to the calibration measurements (see below for details). Then, each A-scan of the re-sampled scan was aligned to a corresponding A-scan in the TD-OCT circular scan. Similarity for each virtual scan was computed by cross correlation, and the re-sampled scan with the highest correlation coefficient was recorded as a matching scan location.

3.1.4 Sampling Circle Calibration

A virtual 3.4mm diameter circle size within 3D SD-OCT volume was adjusted by the calibration measurement of each SD-OCT device. A fake (phantom) eye was used with grid to find the calibration factor of each SD-OCT device (Figure 3-3). SD-OCT fundus image was manually registered to a reference scanning laser ophthalmoscopy (SLO) image by scaling, rotating, and translation. The relative scan size of each device was then determined by measuring the width of the OCT fundus image on the SLO image (Figure 3-3C). The precise window size of each device is summarized in Table 3-2 and visualized in Figure 3-4.

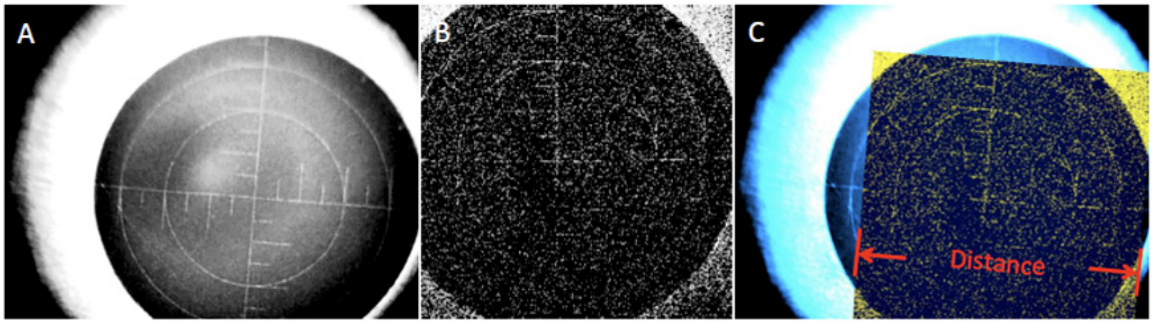

Figure 3-3. Visualization of measuring calibration factor: A) SLO image of phantom eye with grid; B) SD-OCT fundus image of phantom eye; C) superimposed image of both SLO image (A) and SD-OCT fundus image (B).

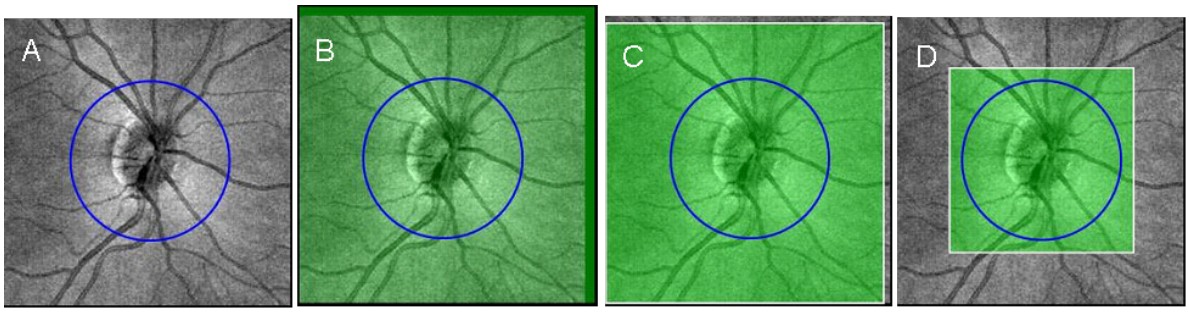

Figure 3-4. Visualization of our current SD-OCT scanning window size: A) ideal 6×6mm scanning window, B) Cirrus 6×6mm, C) Spectralis 6×6mm, D) RTVue 4×4mm.

Table 3-2. Summary of the current scanning window size for SD-OCT devices.

		Cirrus	Spectralis	RTVue
Window Size	Scan Setting	6 × 6 mm (200 × 200 pixel)	6 × 6 mm (512 × 193 pixel)	4 × 4 mm (513 × 101 pixel)
	Actual Size	6.26 × 6.26 mm	5.89 × 5.89 mm	3.88 × 3.88 mm

3.1.5 Performance assessment of the matched scan location

We assessed the accuracy of the matched scan locations by measuring the distance between two center points of TD-OCT circle scan and the matched virtual SD-OCT circle scans. TD-OCT video fundus image was manually registered with the corresponding SD-OCT fundus images by rotating, scaling, and translation according to major retinal vessels (Figure 3-5). The distance between the centers of TD-OCT scan circle and the matched virtual SD-OCT scan circle, was measured on the composite images (Figure 3-5B, 3-5C, 3-5D; blue and white circles).

Additionally, we computed the systematic difference (bias components (α, β)) in RNFL thickness measurement between TD-OCT and SD-OCT devices. These bias components can be used to drive calibration equation between TD-OCT and SD-OCT and between SD-OCT to SD-OCT (Appendix A). For example, the following equation can be used to convert SD-OCT RNFL measurement to TD-OCT RNFL measurement or vice versa.

$$\mathrm{RNFL}_{TD\text{-}OCT} = \left(\alpha_{TD-OCT} - \frac{\alpha_{SD-OCT}\beta_{TD-OCT}}{\beta_{SD-OCT}} \right) + \left(\frac{\beta_{TD-OCT}}{\beta_{SD-OCT}} \right) \times \mathrm{RNFL}_{SD-OCT}$$

When

$$\left(\frac{\beta_{TD-OCT}}{\beta_{SD-OCT}} \right) = 1 \text{ and } \left(\alpha_{TD-OCT} - \frac{\alpha_{SD-OCT}\beta_{TD-OCT}}{\beta_{SD-OCT}} \right) = 0, \text{ there is no bias.}$$

When

$$\left(\frac{\beta_{TD-OCT}}{\beta_{SD-OCT}} \right) = 1 \text{ and } \left(\alpha_{TD-OCT} - \frac{\alpha_{SD-OCT}\beta_{TD-OCT}}{\beta_{SD-OCT}} \right) \neq 0, \text{ there is a constant bias.}$$

When

$$\left(\frac{\beta_{TD-OCT}}{\beta_{SD-OCT}} \right) \neq 1, \text{ there is a non-constant bias.}$$

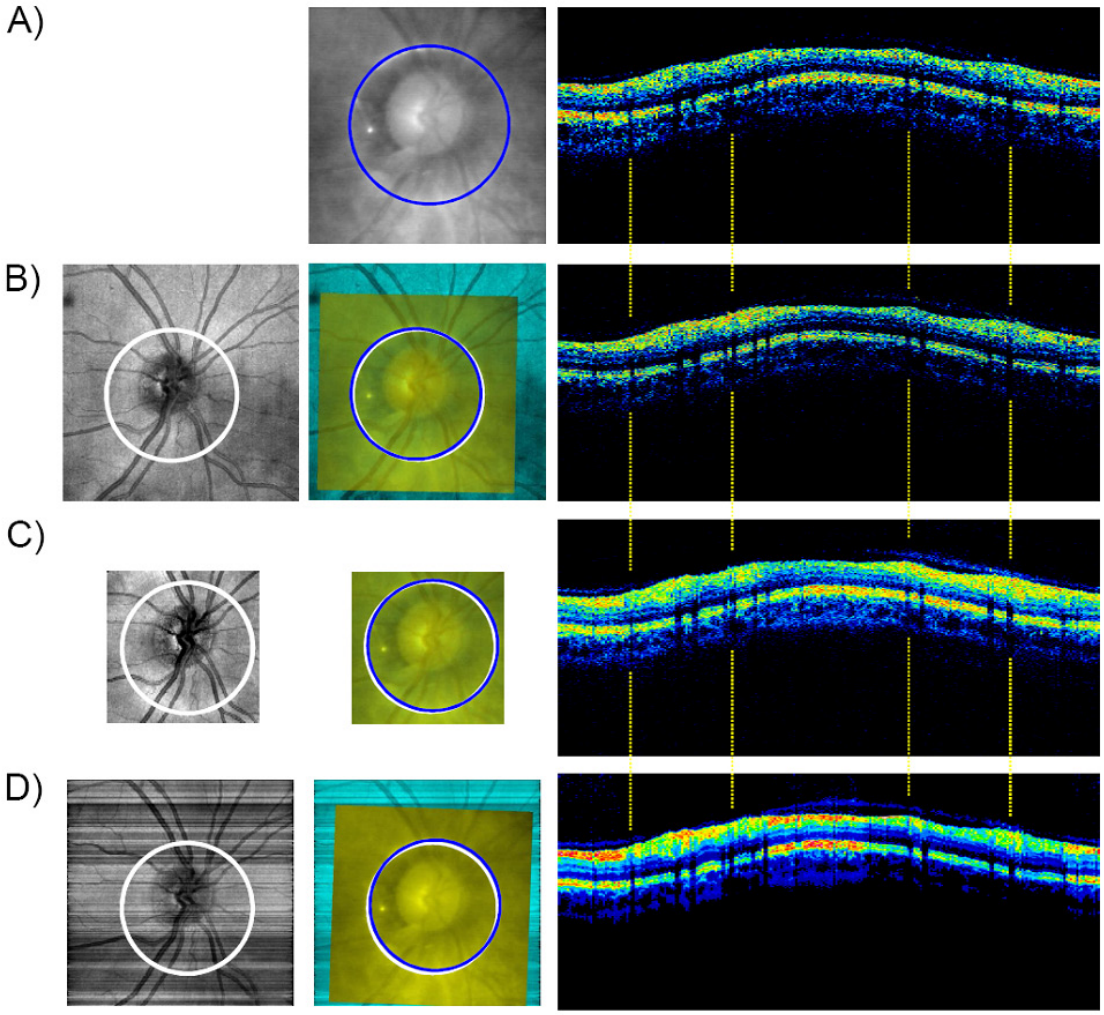

Figure 3-5. Manual registration of TD-OCT video fundus image (A) with SD-OCT fundus images (B, C, and D). Distance between the two circle centers (blue and white) was measured after registration. RNFL thickness measurement from the cross-sectional image was obtained with our own software.

3.1.6 Statistical Analysis

A linear mixed effects model [31-33] was used to assess the constant bias and standard deviation (SD) for the distance between scan center location with TD-OCT and SD-OCT. In addition, a secondary analysis was conducted only with scans where the entire TD-OCT circle was within the smallest SD-OCT scanning window because the dimensions of the scan window varied

among SD-OCT device (smallest window with RTVue; Table 3-1). This subset analysis included an identical set of scans for all SD-OCT devices due to various scanning window size of SD-OCT volume. We used a value of $p<0.05$ as the criterion of statistical significance.

A structural equation model (SEM; Figure 2-6) was used to model the measurement error of the devices. This model describes the relative systematic error (bias) between devices and the random error (imprecision) of each device.

3.2 RESULTS

Subject demographics were summarized in Table 3-3. Healthy eyes had thicker mean RNFL than glaucomatous eyes ($p<0.01$, mixed effects model). No scans were excluded due to either eye motion and/or low signal to noise ratio (SNR) and there was no SLM algorithm failure.

Table 3-3. Patient demographics

	Healthy (N=12)	Glaucoma (N=7)
Male : Female	5 : 7	2 : 5
Age (years)	37.6 ± 10.6	63.2 ± 4.3
TD-OCT RNFL Thickness (μm)	102.8 ± 9.2	88.6 ± 16.5

3.2.1 Distance between the center points

Table 3-4 summarizes the mean and standard deviation for the distance between TD- and matched SD-OCT scan center locations. There was strong interaction between device and

diagnosis except for Cirrus: scan location matching algorithm with Cirrus showed no significant interaction ($p>0.37$). According to the primary analysis results with all qualified scans, the mean distance with healthy eyes was statistically significantly ($p<0.01$) larger for RTVue compared to Cirrus and Spectralis but not between Cirrus and Spectralis ($p>0.22$). The mean distance with glaucomatous eyes was statistically significantly smaller for Cirrus compared to RTVue and Spectralis ($p<0.01$ and $p<0.02$, respectively) but not between RTVue and Spectralis ($p>0.37$). The secondary analysis was performed only with scans completely within 4x4 mm area (RTVue scanning window size) for a fair comparison (Table 3-4). 77 qualified scans of 18 eyes (11 healthy and 7 glaucoma) were included in this subset analysis. The analysis of healthy eyes (41 qualified scans) was almost identical to the primary analysis results (e.g. RTVue showed significantly larger mean ($p<0.04$) of the distance than Cirrus and Spectralis). The mean distance with glaucomatous eyes in the secondary analysis no longer showed a statistically significant difference between Cirrus and RTVue. The imprecision ratios between devices and conditions were also summarized in Table 3-5. The imprecision ratio with identical scans with all devices was lower than all qualified scans and consistent between devices.

Table 3-4. Mean and standard deviation (SD) [95% confidence interval] for the distance between TD-OCT and SD-OCT scan center location. SLM algorithm showed strong interaction between device and condition except Cirrus: its mean was consistent for both healthy and glaucoma.

Analysis Dataset	Device	No. of eyes	Qualified Scans (Healthy: Glaucoma)	Healthy		Glaucoma	
				Mean (μm)	Imprecision SD (μm)	Mean (μm)	Imprecision SD (μm)
All Qualified Scans	Cirrus	19	171 (108: 63)	82.2 [53.7 - 110.7]	71.9 [62.6 - 82.6]	100.6 [64.0 - 137.2]	84.3 [70.1 - 101.4]
	RTVue	19	171 (108: 63)	239.9 [202.2 - 277.6]	148.8 [129.7 - 170.7]	169.1 [129.7 - 208.5]	102.6 [85.7 - 122.7]
	Spectralis	18	162 (99: 63)	95.0 [65.5 - 124.5]	77.3 [66.9 - 89.4]	149.2 [102.3 - 196.2]	145.6 [121.8 - 174.1]
Scans Complete Within 4x4mm	Cirrus	18	77 (41: 36)	94.1 [58.0 - 130.2]	73.1 [57.7 - 92.6]	100.6 [52.7 - 148.5]	91.6 [71.9 - 116.5]
	RTVue	18	77 (41: 36)	144.4 [93.5 - 195.3]	137.6 [109.8 - 172.3]	108.8 [73.7 - 144.0]	60.0 [46.3 - 77.7]
	Spectralis	18	77 (41: 36)	96.2 [62.0 - 130.4]	106.8 [50.0 - 154.1]	154.1 [106.8 - 201.4]	113.5 [88.4 - 145.7]

Table 3-5. Imprecision ratio [95% confidence interval] between devices (Cirrus, RTVue, and Spectralis) and conditions (healthy and glaucoma). The imprecision ratio with identical scans with all devices was lower than all qualified scans and consistent between devices.

Imprecision Ratio	Cirrus		RTVue		Spectralis	
	Healthy	Glaucoma	Healthy	Glaucoma	Healthy	Glaucoma
All Qualified Scans	1.00 (Ref.)	1.17 [0.93 - 1.47]	2.07 [1.70 - 2.52]	1.43 [1.13 - 1.79]	1.08 [0.88 - 1.31]	2.02 [1.61 - 2.55]
Identical Scans Within 4×4 mm	1.00 (Ref.)	1.25 [0.89 - 1.76]	1.88 [1.36 - 2.61]	0.82 [0.58 - 1.16]	0.86 [0.62 - 1.20]	1.55 [1.10 - 2.19]

3.2.2 RNFL thickness measurements comparison

The statistical analysis for RNFL measurement was performed with five out of nine repeated TD-OCT scans (Figure 2-1) in randomized fashion. The corresponding five matched SD-OCT

resampled images were paired with them. Table 3-6 shows the RNFL thickness measurements from four OCT devices: TD-OCT, Cirrus, RTVue, and Spectralis. The calibration equation coefficients (α, β) were computed from the matched SD-OCT images. The scale components (β) of Cirrus, RTVue, and Spectralis were 1.07, 1.26, and 1.26, respectively. In other words, the global mean RNFL thickness measurements of Cirrus, RTVue, and Spectralis were, respectively, 7%, 26%, and 26% higher than TD-OCT circle scan. However, the difference was not statistically significant. Figure 3-6 scatter plot summaries the calibration equations of sectoral parameters: global mean, temporal, superior, nasal, and inferior. The RNFL thickness measurement from TD-OCT is plotted against Cirrus, RTVue, and Spectralis. The calibration equation (solid red) described on Table 3-7 is plotted with the ideal diagonal line (dashed).

Table 3-6. The RNFL thickness measurements from four OCT devices: TD-OCT, Cirrus, RTVue, and Spectralis.

		TD-OCT		Cirrus		RTVue		Spectralis	
		Healthy	Glaucoma	Healthy	Glaucoma	Healthy	Glaucoma	Healthy	Glaucoma
Global Mean		101.6	85.5	115.1	101.2	123.7	100.5	109.9	96.1
Quadrant	Temporal	81.4	79.1	98.7	87.2	109.3	96.0	92.0	90.3
	Superior	125.7	101.6	138.4	120.7	143.5	113.6	129.5	107.7
	Nasal	72.5	64.3	83.8	84.3	100.2	78.2	89.3	76.9
	Inferior	127.0	97.1	139.3	112.5	141.8	114.1	128.7	109.6
Clock Hour	1	60.2	63.6	80.4	70.8	93.3	81.3	77.1	74.9
	2	95.0	94.3	114.9	102.1	123.1	109.4	102.6	100.8
	3	146.3	120.1	163.3	129.2	168.2	131.9	142.4	120.2
	4	119.8	98.5	131.0	113.4	135.6	103.5	121.8	104.0
	5	111.0	86.0	121.5	119.2	127.2	105.4	124.8	99.1
	6	85.1	76.1	104.0	106.0	118.5	98.2	103.9	91.3
	7	61.3	52.8	69.9	67.6	84.5	60.8	78.0	64.9
	8	71.2	63.5	78.4	81.1	97.9	75.9	87.0	75.1
	9	98.2	80.7	107.1	95.1	117.3	92.9	105.7	88.9
	10	131.5	101.0	136.4	115.8	134.8	122.1	123.5	110.6
	11	151.5	109.9	169.0	123.8	170.1	124.1	152.8	125.3
	12	88.6	79.1	110.8	96.0	120.0	103.2	104.9	101.9

Table 3-7. The estimated bias components (α, β) for calibration equation.

Sector		TD-OCT (Ref.)		Cirrus		RTVue		Spectralis	
		α(μm)	β	α(μm)	β [95% CI]	α(μm)	β [95% CI]	α(μm)	β [95% CI]
Global Mean		-3.12	1	15.65	1.07 [0.67-1.72]	-1.42	1.26 [0.71-2.10]	-13.18	1.26 [0.91-1.90]
Quadrant	Temporal	-17.87	1	-5.87	1.00 [0.62-1.39]	16.56	0.90 [0.61-1.21]	6.25	0.86 [0.64-1.11]
	Superior	7.78	1	30.30	1.05 [0.54-2.56]	-33.44	1.55 [0.69-3.83]	-14.19	1.36 [0.77-3.38]
	Nasal	-28.23	1	19.74	0.74 [0.30-1.61]	-6.44	0.90 [0.08-2.29]	9.65	0.56 [-0.01-1.58]
	Inferior	-20.55	1	-10.41	1.00 [0.76-1.27]	10.62	0.87 [0.62-1.14]	17.09	0.77 [0.63-0.94]
Clock Hour	1	-13.06	1	53.77	0.58 [0.06-1.51]	-56.45	1.55 [0.83-3.46]	-10.74	1.08 [0.57-2.48]
	2	-87.66	1	55.39	0.55 [-0.06-1.35]	-107.89	1.11 [0.34-4.63]	46.40	0.45 [-0.04-1.78]
	3	-16.98	1	0.59	1.14 [0.56-2.30]	6.46	0.86 [-0.37-2.08]	9.45	0.69 [0.10-1.45]
	4	-16.67	1	7.59	1.09 [0.61-2.36]	12.69	0.99 [0.16-2.51]	4.55	1.13 [0.60-2.82]
	5	-16.81	1	-3.02	0.98 [0.71-1.35]	8.75	0.93 [0.62-1.31]	9.98	0.83 [0.60-1.14]
	6	-24.19	1	-1.20	0.89 [0.70-1.11]	19.46	0.76 [0.56-0.98]	3.24	0.80 [0.66-0.97]
	7	-11.23	1	-20.65	1.19 [0.97-1.52]	-13.77	1.16 [0.89-1.51]	35.72	0.73 [0.57-0.95]
	8	-10.43	1	-19.11	1.31 [1.02-1.69]	10.22	1.09 [0.79-1.46]	15.89	0.92 [0.63-1.28]
	9	-8.10	1	-0.59	1.12 [0.17-2.94]	5.47	1.19 [0.36-2.87]	2.57	1.03 [0.44-2.62]
	10	-6.54	1	3.14	1.04 [0.69-1.39]	12.17	1.03 [0.75-1.33]	-8.99	1.09 [0.95-1.25]
	11	27.50	1	-22.16	1.62 [1.17-2.35]	-14.96	1.52 [0.87-2.39]	-0.37	1.26 [0.82-1.91]
	12	-3.74	1	0.10	1.16 [0.70-2.38]	-0.85	1.10 [0.41-2.46]	3.95	1.01 [0.62-2.14]

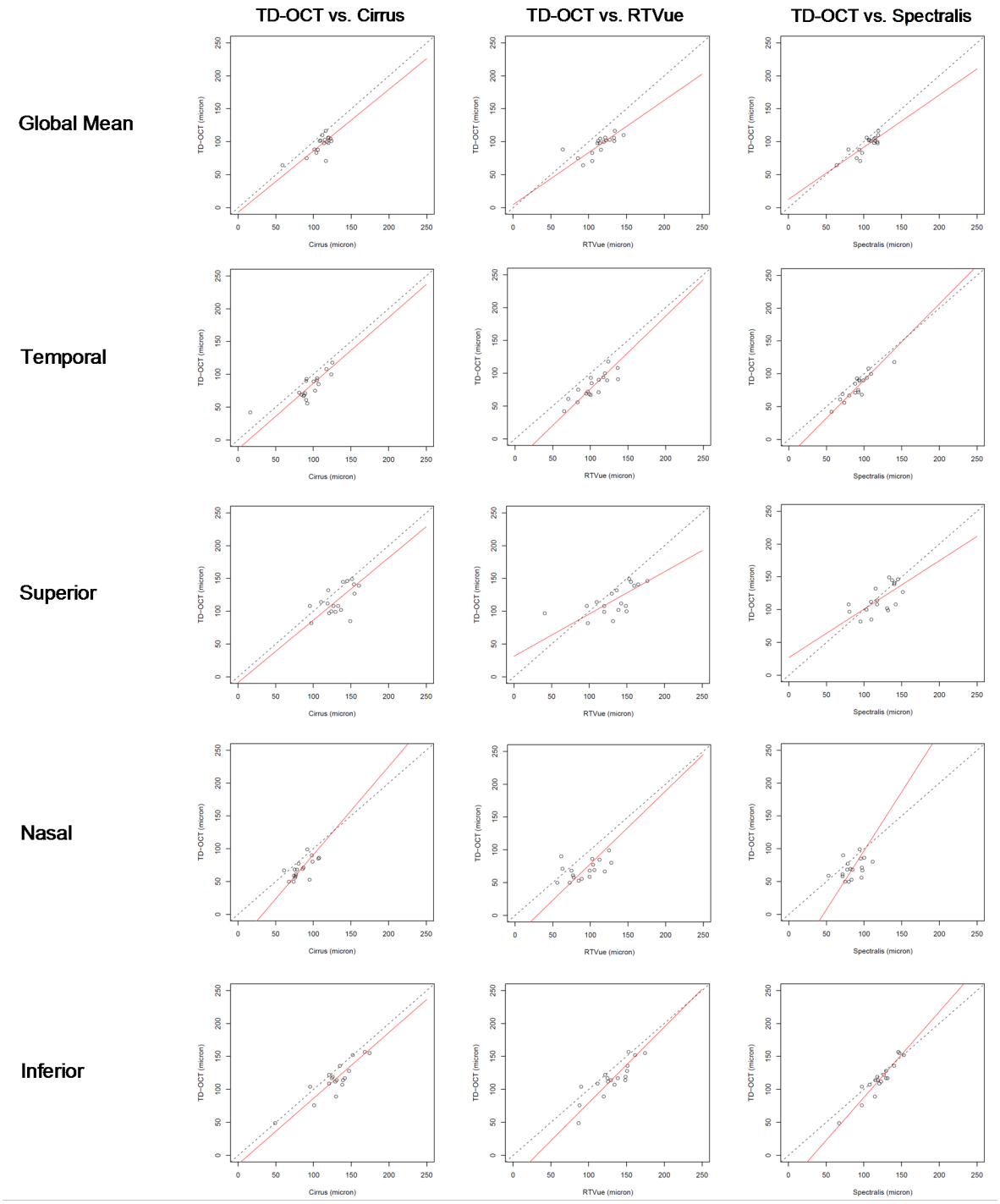

Figure 3-6. Scatter plot of the five sectoral RNFL thickness measurements. The RNFL thickness measurement from TD-OCT is plotted against Cirrus, RTVue, and Spectralis. The calibration equation (solid red) described on Table 6 is plotted with the ideal diagonal line (TD-OCT = Cirrus, dashed).

3.3 DISCUSSION

RNFL thickness measurement needs to be comparable (inter-changeable) between TD-OCT and SD-OCT from various manufacturers in order to ensure a smooth technological transition while maintaining the integrity of longitudinal observations essential to detecting disease progression. In this study, the performance of SLM algorithm was tested on both spatially isotropic and anisotropic SD-OCT volume scans with healthy and glaucomatous eyes. The results showed that the proposed scan location matching algorithm detected the TD-OCT scan location within the corresponding 3D SD-OCT volume scans acquired with various devices in relatively small error (e.g. 144.4 μm on RTVue 3D scan is equivalent to about 3.6 pixels on screen). Therefore, this approach is a strong candidate to bridge the gap between TD-OCT and SD-OCT. Moreover, no external reference information (e.g., fundus image) is required to enable comparability between them with this method.

RTVue scanning window (Figure 3-4) is markedly smaller than other SD-OCT devices that substantially reduced the number of scans where the entire TD-OCT circle was within the SD-OCT window. Therefore, in some cases, SLM algorithm could not find the exact location of TD-OCT circle scan within RTVue volume scan (Figure 3-7). When this happened, we forced the SLM algorithm to select the closest location within the RTVue volume. This may explain why RTVue was relatively less accurate than Cirrus and Spectralis in the primary analysis but not in the secondary analysis.

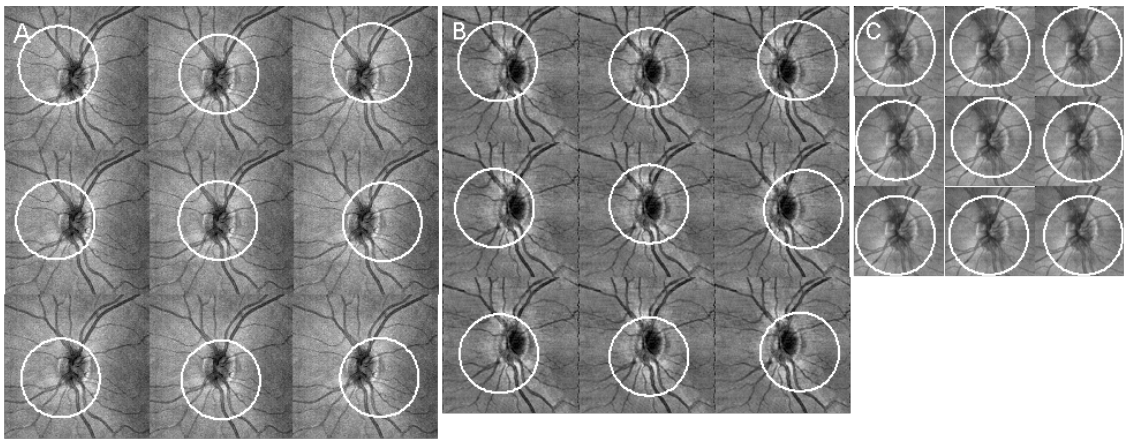

Figure 3-7. Visualization of the various scanning window sizes of SD-OCT: A) Cirrus; B) Spectralis; C) RTVue. SD-OCT fundus image is different between devices by manufacturer. White circle on each SD-OCT fundus image represents a virtual 3.4 mm diameter circle relative to TD-OCT circle scan. RTVue (C) shows relatively small window size and this was a potential problem for SLM algorithm because it was possible that TD-OCT circle scan may be partially missing within RTVue volume due to its small widow size.

In addition, the calibration equation coefficients (α, β) were successfully computed from the matched SD-OCT images. The difference of scale components (β) of Cirrus, RTVue, and Spectralis were not statistically significant. However, we hypothesize that it does not imply that there was no difference because the 95% confidence interval was too wide to be conclusive. This hypothesis is yet to be tested.

In conclusion, the SLM algorithm is robust and can be applied to 3D SD-OCT volume data regardless of different manufactures and scan designs. This method may bridge the gap in RNFL thickness measurements between TD-OCT circular scan and 3D SD-OCT scan data acquired using various units, providing longitudinal comparability between TD- and SD-OCT measurements.

4.0 NORMALIZATION OF TIME DOMAIN-OPTICAL COHERENCE TOMOGRAPHY (TD-OCT) RETINAL NERVE FIBER LAYER THICKNESS MEASUREMENTS BY USING MATHEMATICAL MODEL OF RETINAL NERVE FIBER BUNDLE DISTRIBUTION (RNFBD) PATTERN

Glaucomatous damage occurs along axon bundles and creates localized wedge-shaped RNFL defects on red-free fundus photographs (Figure 1-2, 1-3, and 4-1) because axons originate from the retinal ganglion cells and converge at the ONH. [11-14] The conventional TD-OCT 3.4mm diameter circle scan centered on the ONH (Figure 1-4) enables quantitative analysis of the retinal nerve fiber layer. [13, 16] Furthermore, multiple repeated RNFL thickness measurements using TD-OCT circle scans in different time points are used to detect glaucoma progression. [15]

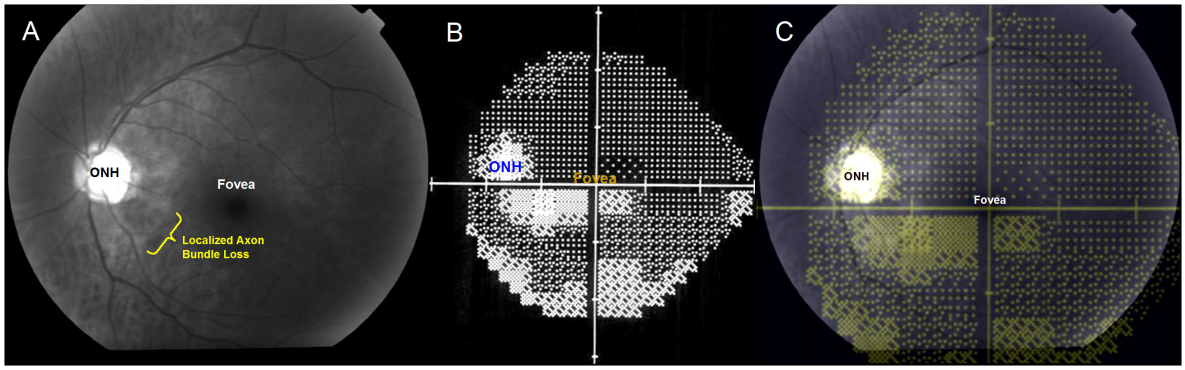

Figure 4-1. Localized axon bundle loss (A) due to glaucomatous damage in human eye can be visualized by red-free fundus photo and VF test (B). Superimposed image (C) shows the correspondence between (A) and (B).

We have established a method to make TD-OCT RNFL thickness measurements in one time point directly comparable to the corresponding SD-OCT RNFL thickness measurements at another time point (Objectives #1 and #2). Hence, longitudinal TD-OCT data can be compared to the present SD-OCT data but not multiple time points together, which are needed for trend (progression) analysis. Scan-to-scan RNFL thickness measurement variability is relatively high mainly due to the operator dependent manual placement of the TD-OCT circular scanning path (variable TD-OCT circular scan locations) (Figure 1-8 and 4-2). [19-21] This prevents us to compare multiple time points together even after scan location matching and proper measurement conversion (both fixed and variable bias).

Retinal nerve fiber bundles form a specific pattern that varies for each individual. A pattern can be generated from a 2D RNFL thickness map of given SD-OCT 3D data. By mathematically modeling the pattern, virtual RNFL thickness values can be computed on any sampling circle location based on the actual values measured in one location. In other words, RNFL thickness measured along an off-centered circle can be normalized to the RNFL thickness virtually sampled along the properly centered circle. This way, multiple TD-OCT RNFL thickness measurements at multiple visits can be made comparable to each other even when the actual scan locations vary.

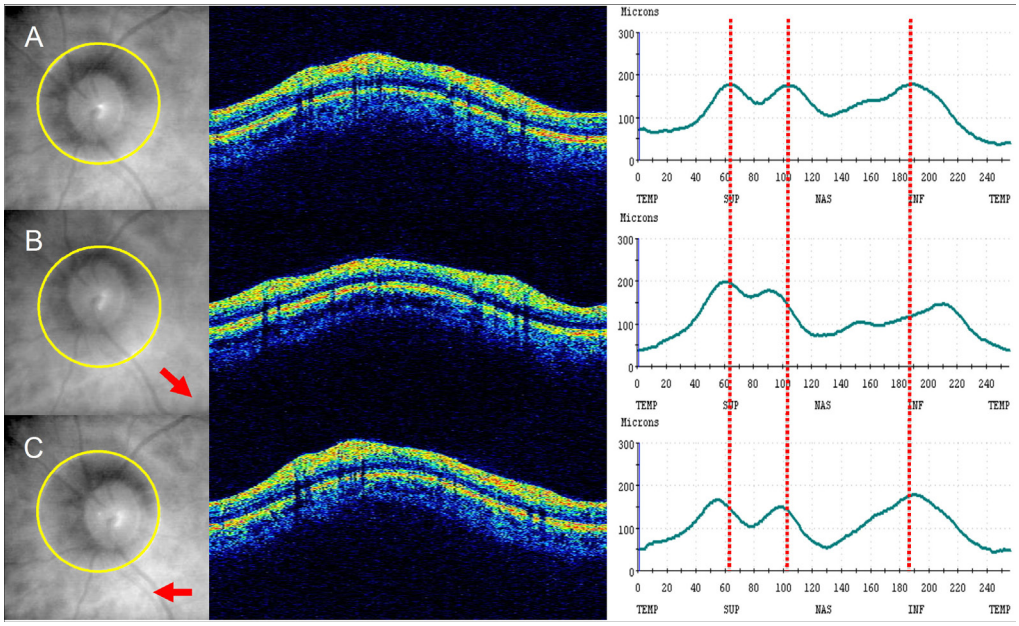

Figure 4-2. One limitation of TD-OCT circular scan: scanning location variation due to the manual placement of the scanning circles. A) a properly centered circle, B) the scanning circle was displaced inferior temporally, and C) the circle was displaced nasally. As a result of displacement, RNFL thickness profile graphs show peak location shifting, and the differences in RNFL thickness measurements.

The aim of this final objective was to develop a mathematical model of the retinal nerve fiber bundle distribution (RNFBD) pattern to normalize the RNFL thickness measurements of off-centered TD-OCT circle scans to a virtual universal location properly centered on the ONH. The reproducibility of normalized RNFL thickness measurement was compared to the actual TD-OCT circular scans (variable scan locations) in order to assess the clinical usefulness of this approach.

4.1 METHODS

We recruited 12 eyes of 12 healthy subjects and 7 eyes of 7 glaucoma subjects from the University of Pittsburgh Medical Center (UPMC) Eye Center. University of Pittsburgh Institutional Review Board (IRB) and ethics committee approval were obtained for the study, and informed consent was obtained from all subjects. This study followed the tenets of the Declaration of Helsinki and was conducted in compliance with the Health Insurance Portability and Accountability Act.

4.1.1 Clinical diagnosis

Inclusion criteria for healthy and glaucoma subjects were identical to the previous study design (section 2.1.1).

4.1.2 Image Acquisition

For this study, the peripapillary region was scanned on all eyes using TD-OCT (StratusOCT; CZMI) and SD-OCT (Cirrus HD-OCT; CZMI) at a single visit. All subject eyes had dilated pupils at the time of OCT scan.

4.1.2.1 TD-OCT

The image acquisition of the TD-OCT 3.4 mm diameter circle scan was identical to the previous study design (section 2.1.2.1). Nine circular scans were obtained from each eye in a single

session by one operator. Each of nine scans had its scanning circle manually centered differently by moving the fixation target (Figure 2-1).

4.1.2.2 SD-OCT

The image acquisition of the 3D SD-OCT volume scan was identical to the previous study design (section 2.1.2.2). ONH margin was detected and then RNFL thickness was measured on every sampling point, except for the area within the ONH, in a fully automated fashion using a software program of our own design. The volume scans with more than 10% of frames labeled as RNFL analysis failure were considered as poor quality scans and discarded. The segmentation failure criteria for virtual OCT slices (or re-sampled images) from the SD-OCT scans was the same as that of the TD-OCT scans.

4.1.3 Mathematical Retinal Nerve Fiber Bundle Distribution (RNFBD) Mapping and Normalization of RNFL Thickness Measurements

RNFL thickness measurements normalization was achieved by utilizing the fact that RNFL thickness decreases along the anatomical RNFBD. [21] Knowing the TD-OCT scan location within the corresponding 3D SD-OCT volume data allows us to adjust RNFL thickness measured on an off-centered circle by tracking the RNFBD to the corresponding point on the virtually centered circle. We assumed the decay along the RNFBD was the same in both time points when TD- and SD-OCT scans were obtained. The detailed flow chart of the normalization is shown in Figure 4-3.

RNFBD map was generated by interpolating the major RNFBD curvatures (one in the superior and another in the inferior hemifield, Figure 4-4C) mimicking the anatomical RNFBD

(Figure 1-7C). Major RNFBD was detected in each hemifield by detecting the center of gravity of the RNFL thickness on multiple resampled RNFL profiles along concentric circles with the diameter ranging from 3.0 to 5.4 mm with 0.015 mm interval centered on the ONH (Figure 4-4C, D, and E). The "raw" major RNFBD information was smoothed by fitting two different curvature models: quadratic ($f(x) = ax^2 + bx + c$) and linear ($f(x) = ax + b$) curves (Figure 4-5). [35] The major RNFBD curvature models, $f(x)$, from superior and inferior hemispheres (Figure 4-4E) were then linearly interpolated, $p(x)$, along concentric circles with a 0.015 mm interval centered on the ONH.

$$p(x) = f(x_i) + \left(f(x_{i+1}) - f(x_i) \right) \times (x - x_i) / (x_{i+1} - x_i)$$

The interpolation of RNFBD curvature was performed only outside the ONH region. In addition, the interpolated lines (Figure 4-5B and 4-5C) were not always quadratic or linear functions because the center of concentric circle was the ONH center instead of the intersection point of the two major RNFBD curvature models (i.e., superior and inferior hemispheres). This was why the individual line on Figure 4-5C does not always look like a linear (i.e., quasi-linear) function.

Using the proposed SLM method, the TD-OCT scan location was identified within the 3D SD-OCT data (Figure 4-6C). Then corresponding points along the virtual centered circle on the SD-OCT data were traced for each sampling point on the off-centered TD-OCT circular scan along the RNFBD map (Figure 4-6F and G). The RNFL thickness ratio (R_U) on these corresponding points (i.e., $a/b = a^*/b^*$ as in Figure 4-6F and G) was then applied to compute the normalized RNFL thickness at each sampling point. The TD-OCT RNFL thickness normalization equation is:

$$b(x, y) = a(x, y) \times Ru,$$
$$Ru = a^*(x, y) / b^*(x, y),$$

Ru: RNFL thickness ratio
a(x, y): RNFL thickness of the off-centered TD-OCT circle scan,
b(x, y): Normalized RNFL thickness at the virtual location on TD-OCT scale,
a(x, y): RNFL thickness at the matched SD-OCT circle scan (SD-OCT scale),*
b(x, y): RNFL thickness at the ONH centered SD-OCT circle scan,*
x, y: X-Y coordinate on the SD-OCT fundus image.

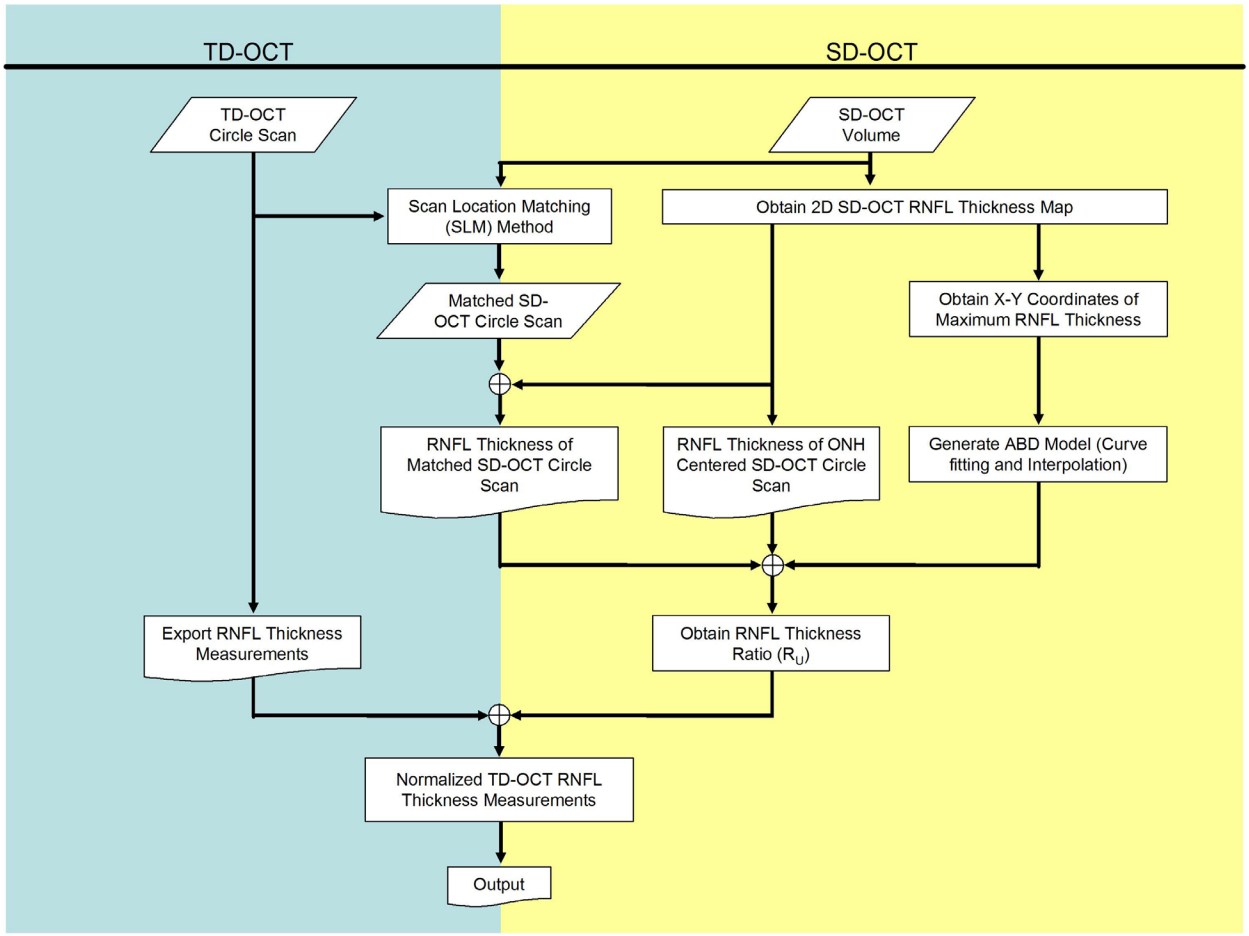

Figure 4-3. **Flow diagram of TD-OCT RNFL thickness measurement normalization process.**

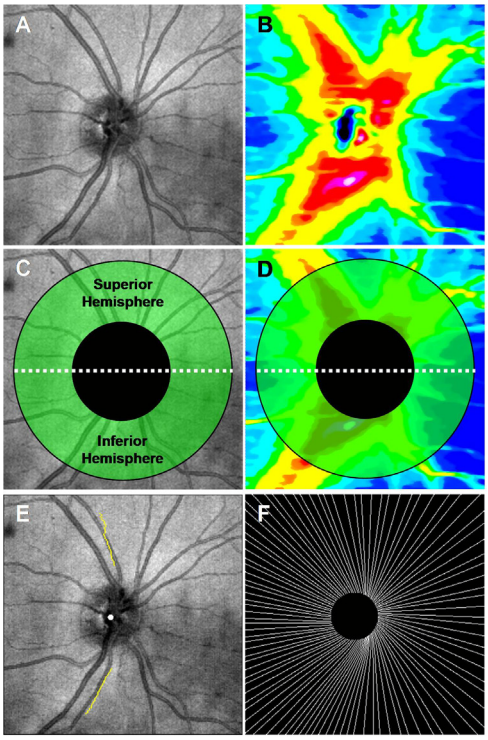

Figure 4-4. Visualization of mathematical RNFBD mapping process: A) 3D SD-OCT volume, B) 2D RNFL thickness map of SD-OCT volume, C) search boundary (green region) for the center of RNFL thickness on SD-OCT fundus image, D) search boundary (green region) for the center of RNFL thickness on 2D RNFL thickness map, E) the computed centers (i.e., center of gravity, yellow line) of RNFL thickness at each radius, F) RNFBD map derived after mathematical interpolation of two fitted curves (E, yellow lines).

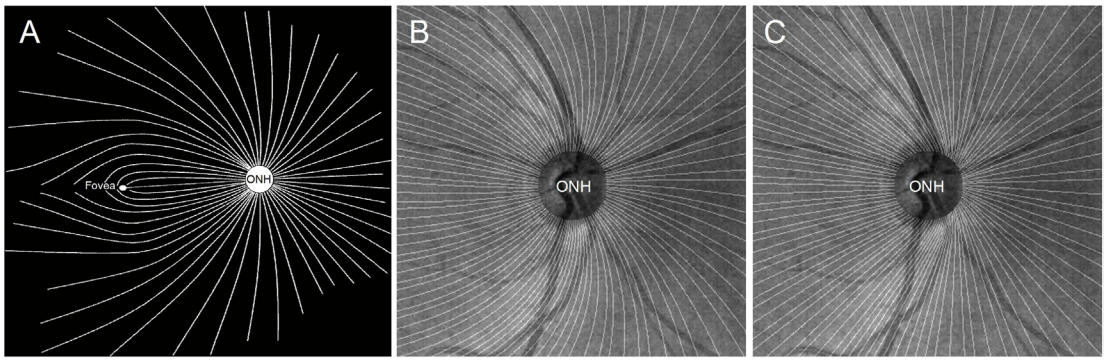

Figure 4-5. Visualization of the two different mathematical RNFBD mapping methods: A) anatomical RNFBD pattern, B) quadratic RNFBD mapping method, and C) quasi-linear RNFBD mapping method. The curvature of each method is different (i.e., quadratic and linear).

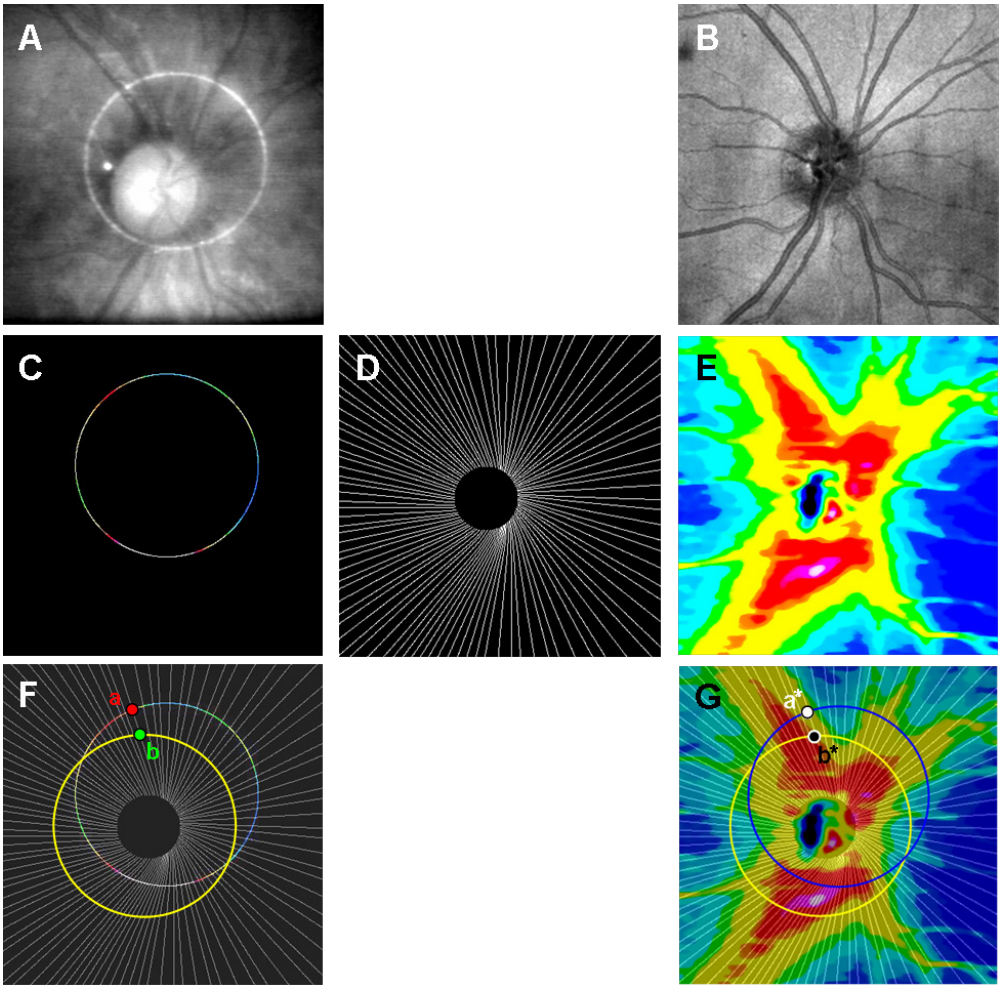

Figure 4-6. Visualization of TD-OCT RNFL thickness measurement normalization process: A) TD-OCT circle scan, B) 3D SD-OCT cube scan, C) matched scan location within SD-OCT cube scan using SLM method and RNFL thickness of (A) in pseudo-color scale, D) axon bundle distribution map, E) 2D RNFL thickness map of (B), F) universal (virtual) location (yellow circle) in TD-OCT scale centered on the optic nerve head, G) universal location (yellow circle) in SD-OCT scale centered on the optic nerve head. RNFL thickness measurement of TD-OCT circle scan at the universal location (F, yellow circle) is computed by using the ratio (R_U) between a/b = a*/b*.

4.1.4 Normalization Performance Assessment

The performance of the RNFL thickness normalization method was assessed by comparing the reproducibility of the global and sectoral RNFL thickness measurements of the following methods: 1) the actual TD-OCT scan with one centered and eight off-centered locations, 2) the quadratic RNFBD normalization method (QM), and 3) the quasi-linear RNFBD normalization method (QLM). The difference between the QM and QLM was the stiffness of estimated RNFBD curves (Figure 4-6).

4.1.5 Statistical Analysis

The reproducibility of the methods was assessed by a structural equation model for the measurement error (Figure 4-7). This statistical model assessed bias and imprecision simultaneously using maximum likelihood estimates of the model parameters along with their corresponding 95% confidence intervals (CI) and p-values. For the analysis, 5 of the 9 scans were selected in randomized fashion.

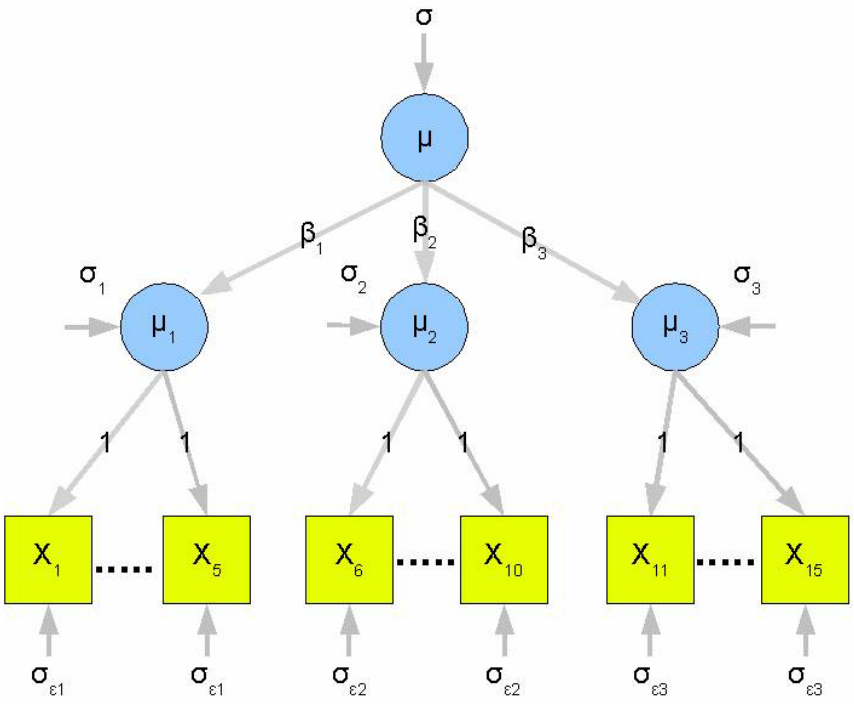

Figure 4-7. Diagram of structural equation model.

4.2 RESULTS

Subject demographics were summarized in Table 4-1. The average RNFL thickness measurement from TD-OCT scans was 104.0 μm (± 9.0 μm) with 12 healthy eyes and 91.5 μm (± 16.3 μm) with 7 glaucomatous eyes (Table 4-2). No scans were excluded due to either eye motion and/or poor signal level and subjectively there was neither SLM algorithm nor RNFBD mapping failure.

Table 4-1. Subject demographics.

	Healthy (N=12)	Glaucoma (N=7)
Male : Female	5 : 7	2 : 5
Age (years)	35.2 ± 11.7	63.2 ± 4.3
TD-OCT RNFL Thickness (μm)	101.8± 9.1	88.6 ± 16.5

Table 4-2. RNFL thickness measurements from TD-OCT circle scan.

Sector		Healthy	Glaucoma
Global Mean		104.0 ±9.0	91.5 ±16.3
Quadrant	Temporal	70.5 ±24.0	70.8 ±13.6
	Superior	118.7 ±28.1	104 ±13.7
	Nasal	93.9 ±33	85.3 ±27.1
	Inferior	132.9 ±21.8	106 ±37.2
Clock Hour	1	56.7 ±23.6	61.1 ±12.2
	2	83.6 ±32.1	79.4 ±21
	3	117.6 ±31.9	116.8 ±27.8
	4	123 ±40.3	102.4 ±20.8
	5	115.2 ±36.8	93 ±17.5
	6	105.1 ±30.4	96.3 ±19.6
	7	83.7 ±33.7	79 ±29.4
	8	93.7 ±38.2	80.5 ±37.9
	9	110.1 ±32.2	101.3 ±48.8
	10	144.3 ±33.5	111.3 ±41.8
	11	144.9 ±34.8	105.7 ±48.3
	12	80.2 ±22.9	77.9 ±26.8

Table 4-3 shows the statistical analysis results of structural equation model. For the analysis, 5 of the 9 scans were selected in randomized fashion. The reproducibility of RNFL thickness measurement between the three different methods (TD-OCT scan, QM, and QLM) was compared. When a ratio is equal to one, the reproducibilities are identical. For example, the estimated reproducibility ratio (QLM/TD-OCT) of global mean RNFL thickness measurements was 0.80 (95% CI 0.63 to 1.02), which indicates that the reproducibility of QLM was 20% better (i.e., the variance was smaller) than for TD-OCT. However, the reproducibilities are not statistically significantly different because the 95% CI includes one. The reproducibility ratios showed that quadratic RNFBD normalization approach statistically significantly improved RNFL thickness measurement reproducibility in comparison with TD-OCT for all sectors except for global mean, nasal quadrant, and clock hour 11. For quasi-linear RNFBD normalization method, the reproducibility ratios were statistically significant in all sectors except global mean.

In addition, the variability of normalized RNFL measurement was close to the previously reported TD- and SD-OCT reproducibility on a different population (Figure 4-8, black solid). [30]

Table 4-3. Comparison of RNFL thickness measurement reproducibility between three methods: 1) the actual TD-OCT circle scan, 2) the quadratic RNFBD normalization method, and 3) the quasi-linear RNFBD normalization method. When a ratio (A/B) is equal to one, reproducibilities are identical. The difference for both methods were statistically significant for all sectors except global mean.

Sector		TD-OCT	Quadratic RNFBD Mapping			Quasi-linear RNFBD Mapping		
		Imprecision SD (μm, A)	β_{QUAD} / $\beta_{TD\text{-}OCT}$	Imprecision SD (μm, B)	Imprecision SD ratio (B / A)	β_{QUASI} / $\beta_{TD\text{-}OCT}$	Imprecision SD (μm, C)	Imprecision SD ratio (C / A)
Global Mean		4.55 [5.31-6.31]	1.03 [0.90-1.17]	4.42	0.83 [0.64-1.08]	0.98 [0.89-1.07]	4.23	0.80 [0.63-1.02]
Quadrant	Temporal	19.86 [17.24-23.18]	1.11 [0.81-1.52]	7.40	0.37 [0.25-0.54]	1.01 [0.89-1.14]	6.21	0.31 [0.24-0.40]
	Superior	19.61 [16.79-23.16]	1.07 [0.74-1.49]	9.50	0.48 [0.32-0.76]	1.05 [0.90-1.23]	10.07	0.51 [0.39-0.68]
	Nasal	24.62 [21.07-29.25]	0.71 [0.26-1.78]	10.92	0.44 [0.16-1.25]	1.07 [0.88-1.30]	7.48	0.30 [0.23-0.41]
	Inferior	19.64 [17.05-22.93]	1.04 [0.87-1.28]	9.15	0.47 [0.35-0.62]	0.94 [0.84-1.04]	8.00	0.41 [0.32-0.52]
Clock Hour	1	27.21 [23.30-32.34]	0.88 [0.53-1.32]	11.79	0.43 [0.26-0.75]	1.02 [0.83-1.21]	16.60	0.61 [0.46-0.82]
	2	26.87 [23.02-31.94]	0.56 [0.13-1.18]	21.80	0.81 [0.35-3.39]	1.01 [0.77-1.28]	11.44	0.43 [0.31-0.60]
	3	24.91 [21.46-29.12]	0.90 [0.43-1.69]	11.21	0.45 [0.23-0.99]	0.94 [0.68-1.27]	11.98	0.48 [0.33-0.72]
	4	25.93 [22.39-30.27]	1.15 [0.67-1.86]	9.38	0.36 [0.21-0.66]	0.91 [0.76-1.10]	10.35	0.40 [0.30-0.53]
	5	30.01 [25.96-35.05]	0.94 [0.63-1.35]	11.23	0.37 [0.24-0.59]	1.04 [0.89-1.22]	10.31	0.34 [0.26-0.45]
	6	35.63 [30.51-42.31]	0.90 [0.55-1.42]	13.27	0.37 [0.22-0.65]	1.03 [0.90-1.17]	10.23	0.29 [0.22-0.37]
	7	22.05 [18.88-25.77]	1.45 [1.16-1.76]	9.38	0.43 [0.32-0.59]	0.95 [0.86-1.05]	14.21	0.64 [0.51-0.83]
	8	27.28 [23.37-32.31]	1.03 [0.70-1.46]	10.83	0.40 [0.26-0.63]	1.03 [0.91-1.17]	10.70	0.39 [0.30-0.51]
	9	15.50 [13.27-18.30]	1.30 [0.72-2.18]	7.14	0.46 [0.25-0.88]	0.95 [0.77-1.18]	9.43	0.61 [0.45-0.83]
	10	25.45 [22.04-29.70]	1.68 [1.12-2.46]	6.52	0.26 [0.16-0.41]	0.94 [0.83-1.06]	12.86	0.51 [0.40-0.65]
	11	21.35 [18.29-25.38]	1.07 [0.65-1.56]	12.54	0.59 [0.36-1.01]	0.97 [0.83-1.13]	12.81	0.60 [0.46-0.79]
	12	30.17 [25.84-35.81]	1.03 [0.63-1.63]	11.25	0.37 [0.22-0.65]	1.02 [0.87-1.18]	12.80	0.42 [0.32-0.56]

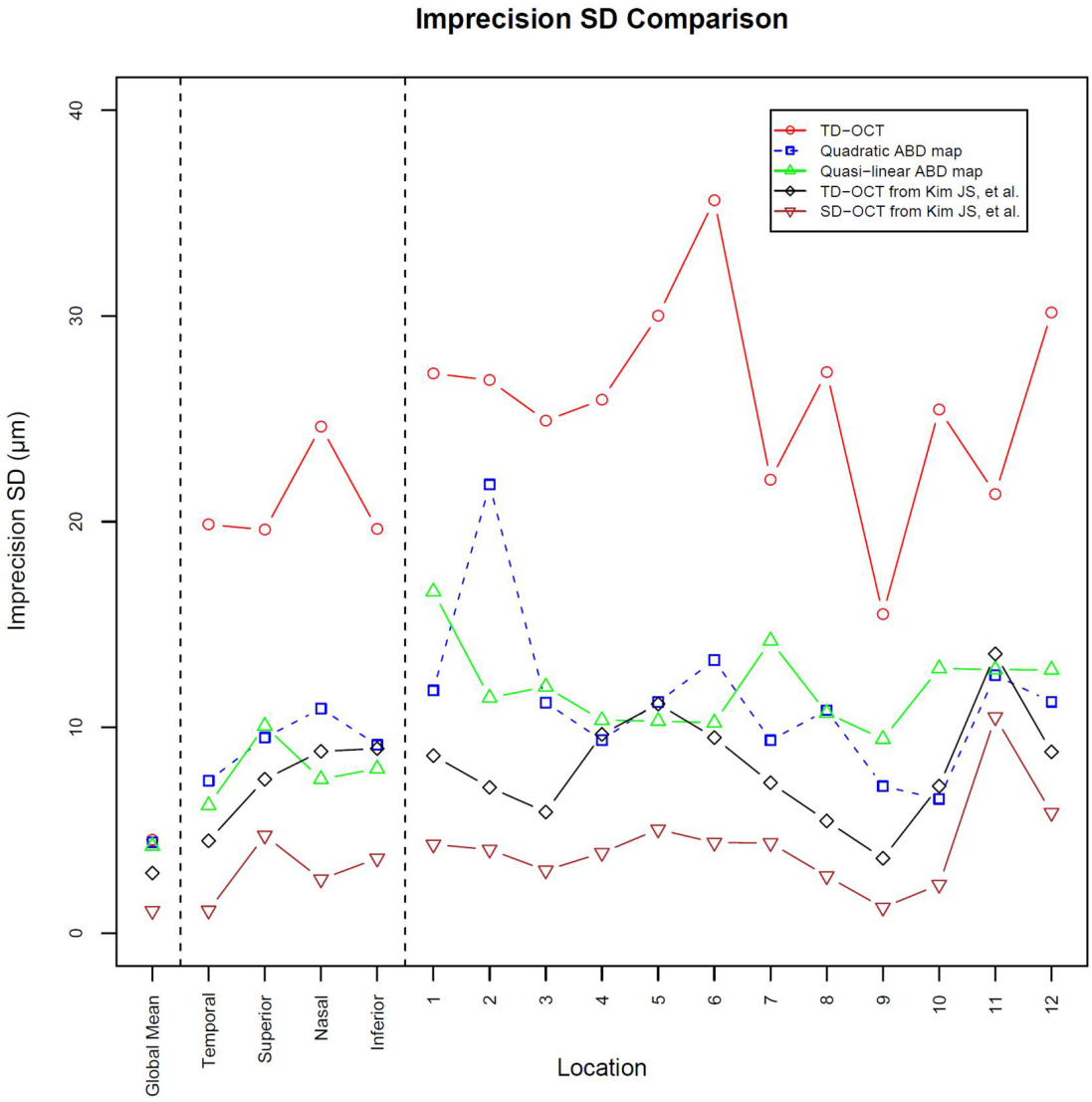

Figure 4-8. The imprecision SD plot. The variability of normalized RNFL thickness measurements was statistically significantly lower than the actual TD-OCT circle scan except global mean. In addition, the variability from *Kim JS, et al.* study (black solid and brown) [30] was plotted for comparison purpose.

4.3 DISCUSSION

We have developed and evaluated an automated algorithm to normalize the RNFL thickness measurement of off-centered TD-OCT circle scan to a virtual properly centered location. The results suggested that our mathematical RNFBD model properly identified the anatomical RNFBD pattern by using the corresponding 3D SD-OCT volume data and improved the reproducibility of TD-OCT RNFL thickness measurements in all sectors except global mean (Table 4-3). Figure 4-10 shows that RNFBD model agrees well with localized defect due to glaucoma. This implies that the multiple TD-OCT RNFL measurements from longitudinal repeated TD-OCT scans can be compared in ideally the same location regardless the accuracy of the actual scan location (Figure 4-2). In other words, this approach made possible for clinicians to track, compare, and detect any retinal changes over a longer period of time with relatively low measurement variation, which may enable more reliable and sensitive glaucomatous progression analysis.

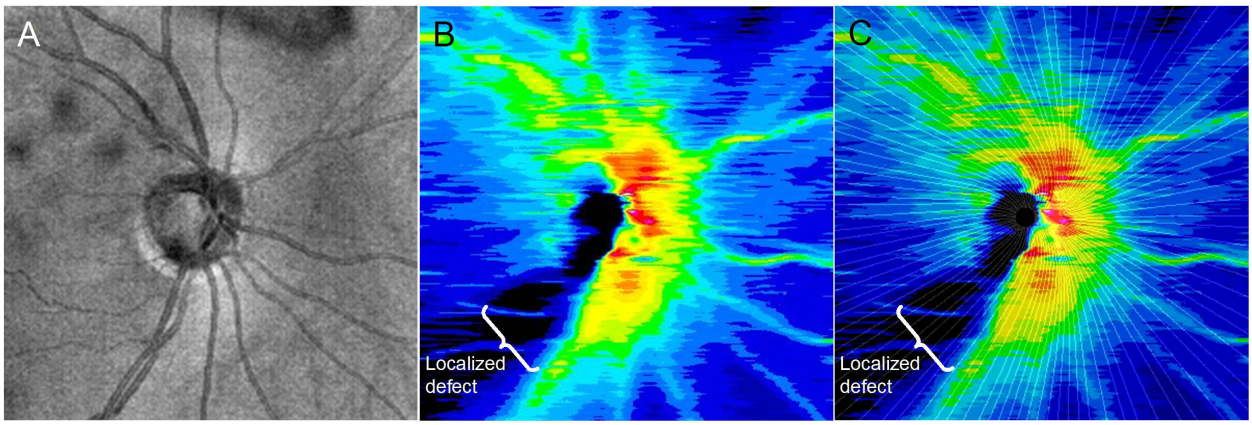

Figure 4-9. RNFBD mapping sample: A) SD-OCT fundus image from a glaucomatous eye, B) 2D RNFL thickness map of SD-OCT from the same eye, and C) RNFBD map superimposed with (B). The localized defect region was marked with white bracket (B and C).

One limitation of the study was that the RNFBD model was based on the RNFL thickness map, which may be altered due to glaucomatous damage. In other words, this method works well with healthy eyes but may not create the best model in eyes with advanced glaucomatous damage. In the present study, since we did not have enough subjects, we did not test the performance difference between healthy and glaucoma groups. Further investigation is needed to check the robustness of this method with glaucomatous eyes.

In terms of the RNFL thickness decay ratio along the RNFBD, we assumed that it stayed the same even with glaucomatous damage because it was calculated along the RNFBD. This assumption also needs to be tested in further investigation.

In conclusion, the RNFL thickness measurement normalization by combining individual mathematical RNFBD models and the SLM algorithm improved reproducibility of TD-OCT RNFL thickness measurements. In addition, this method may provide a useful tool for study of longitudinal glaucoma progression.

5.0 DISCUSSION

In this study, three objectives were achieved to improve the clinical utility of OCT RNFL measurement by establishing data comparability across the OCT technology generations and models. The first objective of this work was to develop and implement an OCT SLM algorithm (PCT/US2009/052951 pending), which finds the precise scan location of the TD-OCT cross-sectional image within the 3D SD-OCT volume from the same eye. The performance of the SLM algorithm allowed the comparison of RNFL measurements in essentially the same location between TD and SD OCT scans, improving agreement and reducing measurement variability. The second objective of this work was to compare the performance of the SLM method on SD-OCT devices that provides spatially isotropic and anisotropic volumes. The performance of the SLM method was tested with healthy and glaucomatous eyes. The results showed that the proposed scan location matching algorithm detected the TD-OCT scan location within the corresponding 3D SD-OCT volume scans, acquired with various devices, with relatively small error (e.g. 144.4 μm on RTVue 3D scan is equivalent to about 3.6 pixels on screen). The performance of SLM algorithm was robust and may be applied to 3D SD-OCT volume data regardless of different manufactures and scan designs. This method may bridge the gap between RNFL thickness measurements acquired with TD-OCT circular scan and 3D SD-OCT scan data, in various units, providing longitudinal comparability between TD- and SD-OCT measurements. Finally, the third objective of this work was to achieve RNFL thickness measurement

normalization of off-centered TD-OCT circle scan, which is the major source of RNFL thickness measurement variation. The results suggested that the normalization method improved reproducibility of TD-OCT RNFL thickness measurements in all sectors including global mean.

The potential limitations of SLM algorithm were: 1) its unselective use of OCT data (e.g., retinal blood vessels are advantageous and stable structure against glaucomatous damage), and 2) the Stratus video fundus images were used to assess the accuracy of scan location matching (i.e., the scan circle appearing on the Stratus video fundus image does not always correspond exactly to its cross-sectional image due to eye motion). The potential limitations of RNFL thickness normalization method were: 1) major RNFBD may not be properly detected on glaucomatous eyes, and 2) RNFL thickness decay ratio may be variable depending on the amount of glaucomatous damage present on a given RNFBD. Despite of these potential limitations, all the presented results of the proposed novel approaches showed significant clinical usefulness. Further development and refinement of these approaches may yield maximum use of legacy OCT data that would otherwise become obsolete.

In summary, this study addressed the importance of "backward-comparability" between the two different OCT technologies and introduced novel methods (i.e., SLM and mathematical RNFBD mapping) to improve the clinical utility of OCT RNFL measurement. Implementing the methods evaluated in this study would help clinicians track, compare, and detect any structural change of the retina over a longer period of time.

APPENDIX A

CALIBRATION EQUATION COMPUTATION

The following calibration equation was modeled with estimating the bias components (α and β) in the RNFL thickness measurement between TD-OCT and SD-OCT,

$$\mathrm{RNFL}_{\text{SD-OCT}} = \underbrace{\left(\alpha_{\text{SD-OCT}} - \frac{\alpha_{\text{TD-OCT}}\beta_{\text{SD-OCT}}}{\beta_{\text{TD-OCT}}}\right)}_{\text{Intercept}} + \underbrace{\frac{\beta_{\text{SD-OCT}}}{\beta_{\text{TD-OCT}}}}_{\text{Slope}} \times \mathrm{RNFL}_{\text{TD-OCT}}$$

$$\mathrm{RNFL}_{\text{TD-OCT}} = \underbrace{\left(\alpha_{\text{TD-OCT}} - \frac{\alpha_{\text{SD-OCT}}\beta_{\text{TD-OCT}}}{\beta_{\text{SD-OCT}}}\right)}_{\text{Intercept}} + \underbrace{\frac{\beta_{\text{TD-OCT}}}{\beta_{\text{SD-OCT}}}}_{\text{Slope}} \times \mathrm{RNFL}_{\text{SD-OCT}}$$

where the ratio of the betas ($\beta_{\text{TD-OCT}}$ and $\beta_{\text{SD-OCT}}$) adjusts for scale differences between the two devices (TD-OCT and SD-OCT), and alphas ($\alpha_{\text{TD-OCT}}$ and $\alpha_{\text{SD-OCT}}$) represent the bias intercepts in the statistical structural equation model (SEM) while the betas represent the regression slopes between the latent variables and the observed variables for each device and location.

Table 4-4 shows the estimated bias and the calibration equation components. When the ratio of the betas equals one and the differences between alphas equal zero, there is no bias. When the ratio of the betas equals one and the difference of the alphas is nonzero, there is a constant bias. When the ratio of the betas differs from one, there is a non-constant bias (i.e., the bias changes with the measurement level).

Table 5-1. The estimated bias (αTD-OCT, αSD-OCT, βTD-OCT, and βSD-OCT) and the calibration equation components (intercepts and slopes) for time domain OCT (TD-OCT) and spectral domain OCT (SD-OCT) retinal nerve fiber layer thickness measurements.

Sector		Bias estimation							Calibration equation			
		TD-OCT		SD-OCT		Ratio: $\beta_{TD\text{-}OCT} / \beta_{SD\text{-}OCT}$			On TD-OCT scale		On SD-OCT scale	
		α	β	α	β	Lower	Est.	Upper	Intercept	Slope	Intercept	Slope
Global Mean		2.51	1.00	-2.51	1.00	0.83	1.01	1.23	5.04	1.01	-4.99	0.99
Quadrants	Temporal	-5.52	1.14	4.46	0.88	0.92	1.30	1.90	-11.30	1.30	8.72	0.77
	Superior	1.61	1.01	-1.64	0.99	0.81	1.03	1.30	3.29	1.03	-3.20	0.97
	Nasal	6.52	0.95	-6.68	1.05	0.65	0.91	1.25	12.59	0.91	-13.87	1.10
	Inferior	11.34	0.92	-12.14	1.09	0.72	0.85	0.99	21.65	0.85	-25.51	1.18
Clock Hour	1	-18.79	1.21	14.92	0.83	0.79	1.47	2.06	-40.71	1.47	27.71	0.68
	2	7.29	0.94	-7.59	1.06	0.66	0.89	1.30	14.04	0.89	-15.80	1.13
	3	-3.86	1.11	3.20	0.90	0.00	1.23	1.94	-7.81	1.23	6.34	0.81
	4	4.75	0.99	-4.76	1.01	0.67	0.99	1.35	9.45	0.99	-9.57	1.01
	5	11.97	0.91	-12.81	1.10	0.70	0.83	1.00	22.64	0.83	-27.20	1.20
	6	12.95	0.91	-14.17	1.10	0.69	0.83	0.97	24.65	0.83	-29.87	1.21
	7	-10.10	1.10	8.99	0.91	0.93	1.21	1.58	-20.98	1.21	17.35	0.83
	8	-2.17	1.09	1.71	0.92	0.75	1.19	1.88	-4.20	1.19	3.54	0.84
	9	-12.77	1.29	9.53	0.78	0.79	1.66	4.76	-28.58	1.66	17.23	0.60
	10	7.13	0.96	-7.25	1.04	0.68	0.92	1.29	13.82	0.92	-14.98	1.08
	11	1.38	1.02	-1.43	0.98	0.49	1.04	1.96	2.87	1.04	-2.75	0.96
	12	13.37	0.91	-14.49	1.10	0.62	0.82	1.24	25.32	0.82	-30.71	1.21

APPENDIX B

ACRONYM, ABBREVIATION, AND SYMBOL DEFINITIONS

2D	two-dimensional
3D	three-dimensional
$\alpha_{TD\text{-}OCT}$ and $\beta_{TD\text{-}OCT}$	bias components of time domain OCT
$\alpha_{SD\text{-}OCT}$ and $\beta_{SD\text{-}OCT}$	bias components of spectral domain OCT
C/D	cup/disc
CCD	charge-coupled device
CI	confidence interval
CSLO	confocal scanning laser ophthalmoscopy
CZMI	Carl Zeiss Meditec, Inc.
GHT	glaucoma hemifield test
HVF	Humphrey Visual Field
IOP	intraocular pressure
IRB	Institutional Review Board
OCT	optical coherence tomography
ONH	optic nerve head

QM	quadratic RNFBD normalization method
QLM	quasi-linear RNFBD normalization method
RGC	retinal ganglion cell
RNFBD	retinal nerve fiber bundle distribution
RNFL	retinal nerve fiber layer
R_U	RNFL thickness ratio
SD	standard deviation
SD-OCT	spectral domain OCT
SEM	structural equation model
SITA	Swedish interactive thresholding algorithm
SLD	super-luminescent diode
SLM	scan location matching
SLO	scanning laser ophthalmoscopy
SLP	scanning laser polarimetry
SNR	signal to noise ratio
SS	signal strength
TD-OCT	time-domain OCT
UPMC	University of Pittsburgh Medical Center
VF	visual field

BIBLIOGRAPHY

1. Huang D, Swanson EA, Lin CP, et al. Optical coherence tomography. Science 1991;254:1178-81.

2. Drexler W, Fujimoto JG. State-of-the-art retinal optical coherence tomography. Prog Retin Eye Res 2008;27:45-88.

3. Schuman JS, Puliafito CA, Fujimoto JG. Optical Coherence Tomography of Ocular Diseases, Second Edition. SLACK, Inc. 2004.

4. Keane PA, Mand PS, Liakopoulos S, et al. Accuracy of retinal thickness measurements obtained with Cirrus optical coherence tomography. Br J Ophthalmol 2009;93:1461-7.

5. Wang M, Hood DC, Cho JS, et al. Measurement of local retinal ganglion cell layer thickness in patients with glaucoma using frequency-domain optical coherence tomography. Arch Ophthalmol 2009;127:875-81.

6. Haeker M, Wu X, Abramoff M, et al. Incorporation of regional information in optimal 3-D graph search with application for intraretinal layer segmentation of optical coherence tomography images. Inf Process Med Imaging 2007;20:607-18.

7. Ishikawa H, Stein DM, Wollstein G, et al. Macular segmentation with optical coherence tomography. Invest Ophthalmol Vis Sci 2005;46:2012-7.

8. Ishikawa H, Piette S, Liebmann JM, Ritch R. Detecting the inner and outer borders of the retinal nerve fiber layer using optical coherence tomography. Graefes Arch Clin Exp Ophthalmol 2002;240:362-71.

9. Mumcuoglu T, Wollstein G, Wojtkowski M, et al. Improved visualization of glaucomatous retinal damage using high-speed ultrahigh-resolution optical coherence tomography. Ophthalmology 2008;115:782-9.

10. Kline LB, Foroozan R. Optic nerve disorders. 2nd edition. Ophthalmology Monograph 10. American Academy of Ophthalmology. New York: Oxford University Press 2007.

11. Grehn F, Stamper R (eds). Glaucoma. (Essentials in Ophthalmology series). Springer, Berlin Heidelberg New York, 2004.

12. Spaeth GL, Eid TM. The glaucomas: concepts and fundamentals. Lippincott Williams & Wilkins 1999.

13. Schuman JS, Hee MR, Puliafito CA, et al. Quantification of nerve fiber layer thickness in normal and glaucomatous eyes using optical coherence tomography. Arch Ophthalmol 1995;113:586-96.

14. Schuman JS. Imaging in Glaucoma. SLACK, Inc. 1997.

15. Wollstein G, Schuman JS, Price LL, et al. Optical coherence tomography longitudinal evaluation of retinal nerve fiber layer thickness in glaucoma. Arch Ophthalmol 2005;123:464-70.

16. Schuman JS, Hee MR, Arya AV, et al. Optical coherence tomography: a new tool for glaucoma diagnosis. Curr Opin Ophthalmol 1995;6:89-95.

17. Ronald Pitts Crick, Peng Tee Khaw. A Textbook of Clinical Ophthalmology: A Practical Guide to Disorders of the Eyes and Their Management. 3rd Edition. Singapore: World Scientific Publishing Company 2003.

18. Adler FH. Adler's physiology of the eye : clinical application / edited by William M. Hart. 9th edition. Saint Louis:Mosby Co., 1992.

19. Ishikawa H, Gabriele ML, Wollstein G, et al. Retinal nerve fiber layer assessment using optical coherence tomography with active optic nerve head tracking. Invest Ophthalmol Vis Sci 2006;47:964-7.

20. Cheung CY, Yiu CK, Weinreb RN, et al. Effects of scan circle displacement in optical coherence tomography retinal nerve fibre layer thickness measurement: a RNFL modelling study. Eye 2008.

21. Gabriele ML, Ishikawa H, Wollstein G, et al. Optical coherence tomography scan circle location and mean retinal nerve fiber layer measurement variability. Invest Ophthalmol Vis Sci 2008;49:2315-21.

22. Sung KR, Kim DY, Park SB, Kook MS. Comparison of retinal nerve fiber layer thickness measured by Cirrus HD and Stratus optical coherence tomography. Ophthalmology. 2009;116:1264-70.

23. Knight OJ, Chang RT, Feuer WJ, Budenz DL. Comparison of retinal nerve fiber layer measurements using time domain and spectral domain optical coherent tomography. Ophthalmology. 2009;116:1271-7.

24. Gonzalez-Garcia AO, Vizzeri G, Bowd C, et al. Reproducibility of RTVue retinal nerve fiber layer thickness and optic disc measurements and agreement with Stratus optical coherence tomography measurements. Am J Ophthalmol 2009;147:1067-74, 74 e1.

25. Kim JS, Ishikawa H, Wollstein G, et al. Retinal Nerve Fiber Layer Thickness Measurement Comparability between Time Domain Optical Coherence Tomography (OCT) and Spectral Domain OCT, Invest Ophthalmol Vis Sci 2009;93:1057-63.

26. Wojtkowski M, Bajraszewski T, Gorczynska I, et al. Ophthalmic imaging by spectral optical coherence tomography. Am J Ophthalmol 2004;138:412-9.

27. Wojtkowski M, Srinivasan V, Fujimoto JG, et al. Three-dimensional retinal imaging with high-speed ultrahigh-resolution optical coherence tomography. Ophthalmology 2005;112:1734-46.

28. Srinivasan VJ, Ko TH, Wojtkowski M, et al. Noninvasive volumetric imaging and morphometry of the rodent retina with high-speed, ultrahigh-resolution optical coherence tomography. Invest Ophthalmol Vis Sci 2006;47:5522-8.

29. Potsaid B, Gorczynska I, Srinivasan VJ, et al. Ultrahigh speed spectral / Fourier domain OCT ophthalmic imaging at 70,000 to 312,500 axial scans per second. Opt Express 2008;16:15149-69.

30. Kim JS, Ishikawa H, Sung KR, et al. Retinal Nerve Fiber Layer Thickness Measurement Reproducibility Improved with Spectral Domain Optical Coherence Tomography. Br J Ophthalmol, 2009. [Epub ahead of print]

31. Pinheiro JC, Bates DM. Mixed-effects Models in S and S-PLUS. New York: Springer, 2000.

32. Demidenko E. Mixed Models: Theory and Applications. New Jersey: John Wiley & Sons, Inc., 2004.

33. Sahai H, Ojeda MM. Analysis of variance for random models: theory, methods, applications, and data analysis. Vol. I. Boston: Birkha¨user, 2004.

34. Tzamalis A, Kynigopoulos M, Schlote T, et al. Improved reproducibility of retinal nerve fiber layer thickness measurements with the repeat-scan protocol using the Stratus OCT in normal and glaucomatous eyes. Graefes Arch Clin Exp Ophthalmol. 2009;247:245-52.

35. Atkinson KE. An introduction to numerical analysis. Second Edition. John Wiley & Sons, Inc. 1989.